The slope of the Baryonic Tully-Fisher relation

Sebastián Gurovich [1], Kenneth Freeman, Helmut Jerjen, Ivânio Puerari[2]

Research School of Astronomy and Astrophysics, Mount Stromlo Observatory, Cotter Rd, Weston, ACT 2611, Australia

Lister Staveley-Smith

School of Physics, University of Western Australia, Crawley, WA 6009, Australia

ABSTRACT

We present the results of a baryonic Tully-Fisher relation (BTFR) study for a local sample of relatively isolated disk galaxies. We derive a BTFR with a slope near 3 measured over about 4 dex in baryon mass for our combined H I and bright spiral disk samples. This BTFR is significantly flatter and has less scatter than the TFR (stellar mass only) with its slope near 4 reported for other samples and studies. A BTFR slope near 3 is in better agreement with the expected slope from simple ΛCDM cosmological simulations that include both stellar and gas baryons. The scatter in the TFR/BTFR appears to depend on W_{20}: galaxies that rotate slower have more scatter. The atomic gas–to–stars ratio shows a break near $W_{20} = 250$ km s^{-1} probably associated with a change in star formation efficiency. In contrast the absence of such a break in the BTFR suggests that this relation was probably set at the main epoch of baryon dissipation rather than as a product of later galactic evolution.

Subject headings: cosmology: observations — dark matter — galaxies: evolution — galaxies: formation

1.   Introduction

The baryonic Tully-Fisher relation (BTFR) for disk galaxies relates the total baryon disk mass to the disk rotational velocity (*e.g.*, Freeman 1999; McGaugh et al. 2000; Bell & de Jong 2001). It has long been recognized that the (luminous) TFR implies a coupling between the

---

[1]Now CONICET fellow at the IATE, Cordoba, Argentina

[2]Sabbatical visit from INAOE, Tonantzintla, Mexico

luminous and dark components of disk galaxies (*e.g.*, Pierce & Tully 1992). Simple cosmological arguments (*e.g.*, White 1997) predict that the slope of the BTFR should be close to 3. In this approach, the galaxy mass is calculated within its virial radius, taken to be the radius r_{200} within which the mean baryon mass surface density is 200 times the critical density of the universe. In its simplest form, the dark halo is modeled as a singular isothermal sphere with a density distribution $\rho(r) = V^2/(4\pi G r^2)$. The only dimensional parameter is the rotational velocity V. It follows that $r_{200} = V/(10H_0)$ where H_0 is the Hubble constant, and the halo mass within r_{200} is $\mathcal{M}_{r_{200,\mathrm{halo}}} = V^3/(10GH_0)$. If some fraction f_d of the halo mass is in the form of gas which becomes the exponential disk of the galaxy, then $M_\mathrm{disk} = f_\mathrm{d}V^3/(10GH_0)$. We would then expect a BTFR with a slope of 3. In this argument, the virial radius within which the mass was estimated is not a structural scalelength of the system in the sense of the scalelength of an exponential disk: it depends on the rotational velocity. This predicted BTFR slope near 3 is also seen in semi-analytic and numerical simulations of galaxy formation within the ΛCDM framework: see Mo & Mao (2000); van den Bosch (2000); Navarro & Steinmetz (2000); Kravtsov et al. (2004).

In reality, it appears that the rotational velocity V of disk galaxies depends on the gravitational fields of both the baryons and the dark matter. V is affected by the structure of the dark matter halo, the initial angular momenta of the baryons and dark matter, the structural evolution of the baryons and the adiabatic compression of the halo by the disk. The stellar and gas baryon masses are affected by baryon loss via winds and other feedback processes, the star formation efficiency and history, all of which vary, possibly in a systematic way, with galaxy mass and environment. Therefore, the slope, zero-point and possible departures from linearity of the BTFR should be sensitive to the many evolutionary processes that go on during galaxy formation from the main epoch of hierarchical assembly until the present time. We should stress that all empirical TF/BTFR studies suffer from the caveat that there is no way yet to measure the rotational velocity at the virial radius, which may be larger or smaller than the velocity inferred from W_{20} measurements (e.g. Battaglia et al. 2005). Also, the baryonic mass may or may not be proportional to the virial mass.

In this paper we derive the TFR and BTFR for a sample of relatively isolated disk galaxies covering a large range in mass and rotational velocity. Our rotational velocity measure is the width W at twenty percent of the peak of the integrated H I profile. In §2 we describe the two samples of galaxies used in this study. In §3 we present the observations and data reduction, and in §4 outline the method of our analysis. §5 contains the results of the observed and derived quantities. In §6 our empirical disk scaling relations are presented and some astrophysical implications are discussed. In §7, we conclude with a summary of the main results of this study. The Appendix includes an overview of the results of similar studies by other authors along with some discussion.

2.   The Sample Selection

We use two local (D < 130 Mpc) field galaxy samples for our BTFR analysis: (i) the Sakai et al. (2000) galaxies with Cepheid distances for the bright end of the relations; (ii) our new H I Parkes All Sky Survey (HIPASS) sample of faint H I-selected galaxies. This second sample selected from the Kilborn et al. (2002) and Koribalski et al. (2004) catalogs was re-observed and contains faint gas-rich galaxies with the following selection rules: (1) none appears to be interacting; (2) absolute magnitude brighter than $M_V = -12.5$; (3) $W_{20} < 290$ km s^{-1}, in order to overlap with the bright end of the TF relation defined by the Sakai sample; (4) inclination $> 40°$ (except one), to reduce errors in our derived velocity widths from correcting for inclination; (5) galactic latitude $|b| > 20°$ (except one); (6) optical diameter $< 2'$ to allow single–pointing imaging in H–band with the CASPIR system on the ANU 2.3–m telescope.

Because the HIPASS positions are imprecise, all optical IDs of our HIPASS sources were verified by Hα spectroscopy with the ANU Dual Beam Spectrograph on the 2.3–m telescope. The spectroscopic observations showed that all the HIPASS sources were correctly identified with the optical counterpart in the NASA Extragalactic Database (NED) except HIPASS J1112-86 that is misidentified in NED as the background galaxy ESO 007- G 004.

3.   Observations and Data Reduction

The HIPASS catalog was our source for the H I selected sample according to the selection rules of §2. However, the HIPASS correlator (with 1024 channels and 64 MHz bandwidth) provided a relatively poor velocity resolution of about 18 km s^{-1} (Barnes et al. 2001) which for a TF/BTF study of faint galaxies with line widths W_{20} as low as 40 km s^{-1} was less than ideal. Therefore new H I observations were obtained with higher velocity resolution for our selected HIPASS galaxies, re–observed with the Parkes 64–m telescope with pointed observations and the narrow–band correlator (1024 channels and 8 MHz bandwidth) that offers a velocity resolution of about 6.6 km s^{-1} after processing. Given that the intrinsic H I velocity dispersions within galaxies ($\sim 6-8$ km s^{-1}) are comparable to the spectral resolution of the HIPASS 8 MHz system, the system was well suited to our needs.

The noise (N) in the H I spectra depend on the resolution and integration time as

$$N \propto \frac{1}{(t\Delta\nu)^{0.5}} \tag{1}$$

where $\Delta\nu$ is the observed frequency resolution and t is the observing time, so we increased the S/N at the higher resolution by combining several individual observations with 24 cycles

of 5 seconds of integration per beam. This gave a total on-source integration time of 14 minutes for the 7 inner HIPASS beams. We combined multiple observations for all our galaxies (except IC 5028) for which the total on-source integration time typically exceeds 30 minutes, typically with a S/N ∼ 10 in peak H I flux.

The individual H I observations were processed through the on-line reduction code LIVE-DATA and multiple data sets for a common source are gridded and combined using the program GRIDZILLA, either at the telescope or post-processed. The MIRIAD package was used for all subsequent H I data analysis. The MIRIAD task `mbspect` was used to produce and measure parameters of the H I spectra including the integrated flux, the systemic velocity and the W_{20} velocity width. The H I spectra were separated from several sources of interference both at the telescope and by post-processing. For example, solar interference that occurred during day-time observations generated baseline distortions which were removed with the MIRIAD task `mbspect` which uses an algorithm that minimizes the mean absolute deviation of the flux-weighted velocities. Tests were performed to determine if the measured velocity widths varied with the degree of hanning smoothing, a parameter that is set in `mbspect`.

Our method for estimating the stellar mass from the light of galaxies used V- and H-band photometric measurements, typically extending over three disk scale lengths. The V-band observations for our H I selected sample were made with the ANU 1–m and 2.3–m telescopes on several nights between 29.03.2001 and 24.06.2003 using two different detectors, the 8K × 8K WFI and the single 2K × 2K imager CCD. The WFI configuration used at the f/8 Cassegrain focus of the 1–m telescope has 8 4K × 2K 3-side buttable CCDs arranged in a 2 × 4 mosaic, with 15 micron pixels and a scale of 0.38 arcsec per pixel. The field of view is 1.2 degrees along the diagonal. We also used the single 2K × 2K thinned CCD at the same focus; it has 24 micron pixels, a scale of 0.6 arcsec per pixel and a field of view of 0.34 degrees along a side. Some V-band images were taken at the Nasmyth focus of the 2.3–m telescope, using the Imager focal reducer and a 1K × 1K CCD with 24 micron pixels, a scale of 0.59 arcsec per pixel and a circular field of view of 6.6 arcmin diameter.

The near-IR H-band observations used the ANU Cryogenic Array Spectrometer/Imager (CASPIR) on the 2.3m telescope on several nights between 05.02.2001 and 08.11.2003. The observations were made at the Cassegrain f/18 focus, using a single 256 × 256 InSb detector array with a field of view of 2 arcmin × 2 arcmin and 30 micron pixels at 0.5 arcsec per pixel. The total on-source integration time for all our H I selected galaxies typically exceeded 30 minutes for both the V and H-bands so that for some of our LSB dwarfs we reached as deep as 26.5 mag arcsec^{-2} in the V-band.

The standard packages of IRAF were used to reduce our V-band data. The individ-

ual processed galaxy frames that were dithered during the observations were registered by measuring the positions of common stars in each frame. We removed any residual intensity offsets with `imsurfit` before combining frames. A plane surface was fitted to the sky: in most cases, a flat (constant) sky level gave the best sky fit. We use the Graham (1982) standards to derive the V-band zero-points, typically accurate to 0.04 magnitudes.

The near-IR observations included sequences of science and sky frames and the reduction was carried out with the `CASPIR` package in IRAF. All the CASPIR frames were linearized except the biases and darks. A normalized flat frame was produced each night and all linearized galaxy, sky, and IRIS standard star frames that were observed on the same night were divided by this normalized flat. Our H-band zeropoints are typically accurate to 0.05 magnitudes. The V-band galaxy frames were geometrically transformed to match the pixel scale and orientation of the corresponding H-band frame using the IRAF tasks `geomap` and `geotran`.

Surface photometry measurements were made on the processed galaxy images. We used the IRAF task `ellipse` to fit isophotal ellipses to the pixel intensity distribution for each galaxy to determine extrapolated magnitudes, scalelengths, ellipticities and colors. The `ellipse` algorithm is described in Jedrzejewski (1987). Usually the V-band data has a higher signal–to–noise. Therefore in all cases except one the isophotal fits were first made on the combined V-band image and then the defined apertures (ellipses) applied to the equivalent combined H-band image. `Ellipse` was run with the center of the first ellipse set to coincide with the geometric center of the galaxy. The position angle and ellipticities of the isophotes were then allowed to vary, keeping the centre fixed, and the isophotes were examined with the IRAF task `isoimap`. This is to confirm that the outer isophotes indeed encompass the fainter parts of the galaxy in both the H and V-bands. We adopted pure exponential disk models for all our galaxies and excluded the inner few data points that in some cases may include a small bar or bulge component. For the literature sample we used published magnitude growth curves that model the galaxy light distributions as pure exponential disk systems. The integrated magnitudes and surface brightness profiles were corrected for galactic extinction using the extinction prescription of Schlegel et al. (1998).

The V-band isophotal ellipticities provide a good estimate of inclination (Macri et al. 2000). For our H I sample we used the mean ellipticity of the three outermost fitted isophotes from the V-band images, and adopted an intrinsic minor–to–major axis ratio $q_\circ = 0.20$. Our inclinations were derived using $\cos^2 i = [(b/a)^2 - q_\circ{}^2]/(1 - q_\circ{}^2)$ where b/a is the isophotal minor–to–major axis ratio with formal inclination errors of typically 3 degrees. The axis ratio values for the Sakai galaxies are from Sakai et al. (2000).

Errors in the apparent magnitudes, integrated H I fluxes, inclinations, W_{20}, distances,

[Fe/H], and gas masses were propagated analytically from the errors in the observations, using conventional techniques. More details of the error analysis are described in Gurovich & Freeman (2007).

4. Methodology

We first calculate our TF and BTF relations using the stellar $\mathcal{M}/L$ adopted directly from McGaugh et al. (2000) which we present in Fig. 3. Then in Fig. 4 we present our relations with the new stellar $\mathcal{M}/L$ obtained from modelling the stellar population histories using the GALAXEV stellar population synthesis (SPS) code of Bruzual & Charlot (2003), described below.

In summary, features of our TF/BTF study include: (1) distances to galaxies without primary or secondary distances derived from large-scale and Virgocentric flow models (see, Gurovich & Freeman 2007) scaled to $H_0 = 73$ km s^{-1} Mpc $^{-1}$; see Gurovich & Freeman (2007) for details. (2) $\mathcal{M}/L$ ratio values derived from GALAXEV SPS models (Bruzual & Charlot 2003) using a bottom light IMF (Chabrier) and a star formation rate that decays exponentially with a timescale constrained by at least one color and metallicity derived from the metallicity–luminosity relation of Mateo (1998); (3) H I observations of the H I-selected galaxies with the 64-m Parkes narrow–band system; (4) detailed Monte Carlo propagation of errors in observed quantities through the entire process to determine our baryon mass errors as described in Gurovich & Freeman (2007); (5) use of Schlegel et al. (1998) extinction values.

The stellar masses are determined for each galaxy with a Monte Carlo implementation of the Bruzual & Charlot (2003) stellar population synthesis (SPS) code. The Bruzual & Charlot (2003) code evolves the stellar population history of a single gas cloud of uniform metallicity. Our goal is to estimate the $\mathcal{M}/L$ values (and errors) for all galaxies, constraining them with the observed colors and adopted metallicities. The color and metallicity values also have known errors and so for each galaxy we run a set of SPS models, choosing the color and metallicity from the gaussian adopted probability distributions associated with the errors. This generates a probability distribution of $\mathcal{M}/L$ values for each galaxy. We choose the age (*i.e.*, the lapsed time since star formation began) that reproduces the observed galaxy colors, restricting them to be between 8 and 13.75 Gyrs to be consistent with the observed ages of the old disk stars in Local Group galaxies (e.g., Mateo 1998). The metallicity for each galaxy is adopted from the literature (when available), or determined by interpolating a weighted bivariate linear fit: $[Fe/H] = a + bM_V$, to the Mateo (1998) L-Z dwarf data with FITEXY (Press et al. 1992). Fig. 1 shows the Mateo L-Z data with weighted fit that we use

to estimate the error in our interpolated [Fe/H] values using Equation 2. The σ_{ab} covariance term of Equation 2 is negative and similar in magnitude to the sum of the three positive terms so the expected error in our metallicity values is small. For each galaxy, the [Fe/H] error values are set to be the standard deviation of the [Fe/H] probability distribution for the Monte Carlo stellar population synthesis simulations. The errors in our [Fe/H] values are calculated from the errors in the M_V values and from the calculated parameters of the fitted L-Z relation, where, $a = -3.8$, $b = -1.7 \times 10^{-1}$, $\sigma_a^2 = 1.4 \times 10^{-2}$, $\sigma_b^2 = 6.0 \times 10^{-4}$ and $\sigma_{ab} = -9.2 \times 10^{-3}$, and:

$$\sigma[\frac{Fe}{H}]^2 = \sigma_a^2 + M_{\rm V}^2 \sigma_b^2 + b^2 \sigma_{M_{\rm V}}^2 + 2 M_{\rm V} \sigma_{ab} \tag{2}$$

The SFR of our models is: $\psi(t) = 1[\mathcal{M}_\odot + \epsilon \mathcal{M}_{\rm PG}(t)] \tau^{-1} \exp(-t/\tau)$, where $\mathcal{M}_{\rm PG}(t) = 1 \mathcal{M}_\odot [1 - \exp(-t/\tau)] - \mathcal{M}_{\rm stars} - \mathcal{M}_{\rm remnants}$ is the mass of gas processed into stars and returned to the ISM and ϵ is the fraction of this gas allowed to recycle into new star formation. In our models, we do not include gas recycling or infall, so we set $\epsilon = 0$. We make this simplification because we wish to treat our galaxies uniformly, even though this assumption is more likely to be true for dwarfs with shallower potential wells than for spirals.

Each galaxy is modelled to cover a wide range of possible star formation history with a Chabrier IMF and star formation rate (SFR) that decreases exponentially in time. For each galaxy we consider star formation histories with different e-folding timescales, selecting values between τ=0.1 and 14 Gyr. Larger values of τ have a nearly constant SFR history and smaller τ values are close to a single burst history. The observational constraints to the BC03 code are the input colors and [Fe/H] values. The errors on colors and [Fe/H] values are determined analytically from the observed and derived parameters, and are assumed to have gaussian probability distributions (Gurovich & Freeman 2007). Linear interpolations were made over the BC03 output grid of discrete [Fe/H], color, $\mathcal{M}/L$, and age values, because the 'observed' input values usually do not fall on the BC03 grid. To calculate the errors in the output $\mathcal{M}/L$ values at a given τ, the simulations for each galaxy were rerun about 100 times, each time using a new input pair of values for color and [Fe/H] selected from their gaussian error distributions. In this way, a distribution of $\mathcal{M}/L$ value was produced for each galaxy. The mean of the $\mathcal{M}/L$ values over all runs, given the age restriction described above, is chosen and the $\mathcal{M}/L$ error is taken to be the standard deviation about the mean of all $\mathcal{M}/L$ values at a given τ. For each galaxy this process is repeated for the range of $\tau-$values, as above, and the mean of all $\mathcal{M}/L$ values is adopted to be our final $\mathcal{M}/L$ value with error given by the standard deviation about the mean of all $\mathcal{M}/L$ values.

The SPS models for our H I selected galaxies are constrained with $(V - H)$ colors measured at the half-light radius because the half-light photometry is more precise than at larger radii. The apparent magnitudes and colors are corrected for galactic extinction following Schlegel et al. (1998) and shown in Tab. 7. The V and H-band photometry give two partly independent estimates of the stellar mass. The total luminosity of the galaxy in each band is derived by extrapolating its radial surface brightness profile, and the stellar mass is then estimated using the derived $\mathcal{M}/L$ values from the SPS simulations. Even though the theoretical H-band $\mathcal{M}/L$ values are probably better estimates of the true $\mathcal{M}/L$ values because of the added sensitivity towards the older stellar populations and the fact that near-IR bands are less effected by extinction, in practice the H-band surface photometry is not as deep, due to the inefficiency of near-IR detectors. Therefore, as a compromise between induced photometric errors and SPS model errors, we choose the weighted mean of the stellar mass values, calculated using $\mathcal{M}/L$ and luminosity values for a minimum of two bands, so the adopted disk mass (stellar) is the weighted mean of the V and H-band disk masses.

Similarly, the stellar mass estimates for the Sakai galaxies are determined by constraining the stellar population histories using $(V - H)$ and $(V - I)$ colors and with metallicities obtained from the literature, with references shown in Tab. 2. The adopted stellar masses for these galaxies are taken to be the weighted mean of all four stellar mass estimates except for NGC 3319 and NGC 4548 for which only two $\mathcal{M}/L$ values could be calculated.

The gas (atomic) masses are determined following equations (3) and (4) to account for He and the heavier elements.

$$\mathcal{M}_{\mathrm{H\,I}} = 2.36 \times 10^5 D^2 F_{\mathrm{H\,I}} \tag{3}$$

where $F_{\mathrm{H\,I}}$ is in Jy km s^{-1} and D is in Mpc.

$$\mathcal{M}_{\mathrm{gas}} = 1.4 \times \mathcal{M}_{\mathrm{H\,I}}. \tag{4}$$

Inclusion of the available H_2 gas component for 6 of the Sakai galaxies did not have a significant effect on the TF/BTFRs; because molecular gas masses are not available for the HIPASS sample, we do not include molecular gas in our baryonic masses.

5. Results

The integrated H I flux values for the Sakai galaxies are tabulated in Tab. 1. These fluxes are not listed in Sakai et al. (2000) but come from several sources in the literature. The weighted mean of the literature values is calculated and found to have a typical error of 25%. The distances to the Sakai galaxies are from Sakai et al. (2000) and the metallicities

for the Sakai galaxies are taken from the literature. Along with the derived gas mass and luminosity values, the reference list is presented in Tab. 2. The W_{20} values for the Sakai galaxies (corrected for inclination and redshift) are from table 2 of Sakai et al. (2000). A redshift correction is not included for our other two galaxy samples because the effect on W_{20} is negligible within our redshift range. Tables 2, 3, 4 and 5 list the derived quantities for the Sakai galaxies including the [Fe/H], stellar $\mathcal{M}/L$s, stellar masses, gas–to–star fractions and mean baryon mass surface density values (see §6.2). Tables 6 and 7 list the surface photometry measurements for our H I selected galaxies. Other measured and derived optical and H I quantities can be found in Tables 8 and 9. Our H I flux values are in good agreement with the HIPASS literature values, our typical v_{helio} errors are about $5\,\mathrm{km\ s^{-1}}$ and our W_{20} measurements have typical errors between 5 and $10\,\mathrm{km\ s^{-1}}$. The baryon mass values including gas–to–star ratio and mean baryon mass surface densities are also tabulated in Tables 10 and 11 and used for our relations in subsequent figures.

We compare our $\mathcal{M}/L$ for our two galaxy samples with the range of modelled $\mathcal{M}/L$ with Scaled Salpeter IMF found in table 3 of Bell & de Jong (2001), for which we constrained 297 and 531 models with our $(V - H)$ and $(V - I)$ colors. As is evidenced in Fig. 2 our $\mathcal{M}/L$ values coincide with the higher probability density bins of the Bell & de Jong (2001) output $\mathcal{M}/L$ grid (in contours). Our models therefore, which include color, IMF, ages, and [Fe/H] constraints, produce $\mathcal{M}/L$ values that are consistent with those adopted by Bell & de Jong (2001) in their scaled Salpeter IMF models. The same IMF was used to construct their preferred BTFR. We note that systematically higher $\mathcal{M}/L$ values that could result from a different universal IMF scaling will act to steepen a BTFR, since the effect of any differential gas–to–star fraction trend with W_{20} , would be diluted. We explore this effect by scaling our modelled $\mathcal{M}/L$ later in Sec. 8.1.

The errors in the baryon mass values depend on the errors in (i) $\mathcal{M}/L$ (obtained from the stellar population synthesis models), (ii) apparent magnitudes, (iii) H I fluxes, and (iv) flow model distances. The $\mathcal{M}/L$ errors themselves include errors in the observed colors and metallicities; errors from the limitations of the stellar population history models have not been included. For galaxies without primary distances, the distance errors are the largest fractional error contribution and can provide up to 30% of the total baryon mass error. Next are the errors in the $\mathcal{M}/L$, then the H I flux errors, and finally the apparent magnitude errors provide the smallest contribution to the baryon mass error budget. See Gurovich & Freeman (2007) for more details. We note that the analysis for the Sakai galaxies shows that the stellar masses are only weakly sensitive to the the color constraint chosen, so the chosen color does not significantly alter the slope of the BTFR. This is consistent with what is found by Bell & de Jong (2001).

6. TF/BTFR

Our TF/BTFR spans four orders of magnitude in stellar mass, from 1.1×10^7 to 1.6×10^{11} $\mathcal{M}_\odot$. Both the baryon mass and the W_{20} values have errors, so we determine weighted bivariate fits with FITEXY from Press et al. (1992), as well as weighted forward and reverse linear least squares fits. We present two versions of the TF/BTFR. The first is derived using the constant stellar $\mathcal{M}/L$ values directly from McGaugh et al. (2000) and the second uses our SPS stellar $\mathcal{M}/L$ values: see Figs. 3 & 4 respectively. A comparison can be found in Tab. 12. In both cases, separate fits are shown for each sample, and for the combined Sakai and H I samples. Qualitatively the fits in both figures are similar. When the H I gas is included, the BTFRs become flatter and the scatter is reduced. Our fits do not change significantly when we correct our W_{20} values for an H I velocity dispersion of 6 km/s, following equation 1 of Swaters et al. (2003), so we do not correct for the velocity dispersion of the gas. We note for comparison that forward and reverse BTFR fits for the Sakai galaxies computed by a least squares routine that derives the error in slope from the weighted residuals of data points about the fitted line in $\mathcal{M}$ and separately in W_{20} are 2.9 ± 0.3 (forward) and 3.1 ± 0.3 (reverse) and for the combined sample both the forward and reverse BTFR weighted fits are calculated to have slopes of 3.1 ± 0.1. If we remove NGC 1365, the most massive outlier galaxy, then the weighted BTF slopes for the Sakai sample alone are 2.7 ± 0.3 (bivariate), 2.6 ± 0.1 (forward) and 2.7 ± 0.1 (reverse). The BTFR slopes for the combined sample, with or without NGC 1365, are all (bivariate, forward and reverse) calculated to be 3.1 ± 0.1. The combined sample appears to provide a consistent estimate of the BTFR slope.

We find that the scatter in the TFR/BTFR is larger for galaxies at lower W_{20} and compare the scatter in Fig. 4 for galaxies with $1.8 < \log W_{20}$ (km/s) < 2.2 and $2.4 < \log W_{20}$ (km/s) < 2.8 by calculating the ratio of the reduced χ^2 values (defined in the usual way) for these two intervals. For the TFR and BTFR the ratios are 2.6 and 1.6 respectively.

Our H I selected sample is weakly biased towards systems of lower W_{20}, which are detected at a higher S/N for a given H I flux. The Sakai et al. (2000) galaxies are mostly large, nearby, modeled with multiple colors and so are relatively free of systematic effects.

The accurate Cepheid distances for the Sakai sample lead to a tight stellar mass TFR with a slope of 4.3 ± 0.4, using our SPS models. This is similar to the typical H-band luminosity TFR slope (4.4 ± 0.3) and confirms that the H-band luminosity is indeed a fair measure of the stellar mass in massive disks. The BTFR for the Sakai galaxies is flatter and even tighter than the TFR, with a slope of 3.1 ± 0.3 (see Tab. 12), close to the value expected from cosmological arguments. This result, that even for the brighter galaxies, the H I mass fraction increases sufficiently with decreasing W_{20} to cause the marked flattening between the TFR and the BTFR was somewhat surprising and is discussed later in the paper. The

BTFR slopes for the H I selected sample, the Sakai sample, and the two samples together are all similar and close to 3.

6.1. Gas Fraction

With the stellar mass estimates from our population synthesis analysis and our H I mass values, we show in Fig. 5 how the gas–to-stars ratio (r_g) defined as $\mathcal{M}_\mathrm{gas}/\mathcal{M}_\mathrm{stars}$, varies with W_{20}. The errors in r_g for the two samples are similar and relatively small because the ratios are distance-independent. The large scatter for galaxies with lower W_{20} appears to be real and is presumably a consequence of variable star formation efficiency. The brighter disk galaxies show rapidly decreasing r_g values with increasing W_{20} (see also Geha et al. (2006). The transition from the decreasing r_g values for the bright galaxies to the roughly constant values for the fainter galaxies occurs near $\log W_{20}$ (km/s) $= 2.4$. This transition value, which appears to mark the change in star formation efficiency, is discussed below.

6.2. Baryon Surface Density

At Joe Silk's suggestion, we used the stellar masses from our SPS models to examine how the mean baryon mass surface density Σ_b, depends on W_{20}. We have only integrated H I masses for our galaxies, and so assume that the H I in each galaxy has an exponential distribution with scalelength equal to the optical scalelength (h). The adopted optical h is taken to be the mean of the V and H-band, h for the H I selected sample and our re-calculated V-band h values from the brightness profiles of Macri et al. (2000) for the Sakai et al. (2000) galaxies. The mean baryon mass surface density estimator is then $\Sigma_b = \mathcal{M}_\mathrm{baryons}/2\pi h^2$. Fig. 6 shows that the surface density Σ_b has a roughly linear dependence on W_{20} .

In estimating Σ_b, we assume that the H I and light have the same scalelength. However, it is likely that the ratio of the H I size of the galaxy to its optical size increases towards fainter systems. This would tend to somewhat steepen the slope of the $\Sigma_b - W_{20}$ relation. To explore this further, we modelled the effect for the sum of two exponential disks: stellar and H I. We assume from Fig. 5 that the stellar and H I mass values for a given dwarf are equal, take the ratio of scalelengths $h_\mathrm{H\,I}/h_\star = \gamma$, and the mean surface brightness inside the half-light radius to be $\mathrm{R_e}$, a parameter commonly used for more general surface brightness distributions. Tab. 13 shows how $\mathrm{R_e}/h_\star$ and Σ_b within $\mathrm{R_e}$ change with γ. This analysis shows that if γ increases as W_{20} decreases, then we would get an increase in the slope of $\log \Sigma_b$ vs $\log W_{20}$ from ~ 1 to ~ 1.3.

7. Summary and Conclusions

We choose a sample of isolated disk galaxies ranging from faint dwarfs to bright spirals. We construct TF and BTF relations and explore the difference between the theoretically predicted BTFR slope of 3 and the TFR slope of 4 obtained by many observers. Regarding this difference, van den Bosch (2000) argued that "the physics regulating star formation and feedback, coupled with the mass dependence of halo densities and stellar populations has to tilt the TF relation to its observed slope. The introduction of a stability-related star formation threshold density increases the slope of the TF relation ...". Our results are entirely consistent with this argument. As W_{20} decreases, the increasing gas–to–stars ratio and decreasing mean baryon mass surface density, possibly associated with a decreasing trend in star formation efficiency, generate the "tilt" between the TFR and the BTFR.

We show the gas–to–stars ratio for our combined sample, and the break at baryon masses near 1 x $10^{10} \mathcal{M}_{\odot}$. Because the BTFR shows no such break, and its slope is close to that expected from cosmological arguments, one could argue that the total baryon content of isolated disk galaxies (as measured by stellar + H I mass) has not been much affected by galaxy evolution, including star formation history. In this sense, the BTFR would be a fundamental relation relating back to the main epoch of galaxy assembly.

There are some systematic uncertainties which affect any discussion of the BTFR. (1) A problem inherent to any TF study is the change in H I profile shape with W_{20} (Noordermeer & Verheijen 2007) and therefore an uncertainty in how to relate W_{20} to the rotational velocity V across the whole range of W_{20} values. (2) We have not included ionized or molecular gas in the total baryonic masses. The idea of large amounts of molecular gas in the dwarfs seems unlikely (*e.g.*, Pilyugin et al. 2004; Read & Trentham 2005). However, a larger fraction of ionized undetected baryons in the more massive galaxies would steepen the slope of the true BTFR. This ionized (warm) gas in the more massive galaxies (*e.g.*, Maller & Bullock 2004; Fukugita & Peebles 2006) may turn out to be more significant in this respect.

8. Appendix: Recasting the TFR

Aaronson & Mould (1983) were amongst the first to observe a bandpass-dependent luminous TFR slope, which has been determined to steepen from ~ 3 in the blue to ~ 4 towards the near-IR (*e.g.*, Sakai et al. 2000). The search was soon on for a band-pass independent slope that attempted to include all baryons. In the Appendix, we discuss the range of published BTF (gas + stars) slopes available in the literature and we attempt to

explain the reason behind some of the discrepancies in these measured values.

However, the fitted BTF and TF parameters that result from most observational studies do not include confidence intervals, determined from robust statistical methods, so the task of comparing parameters quantitatively is not attempted here. Instead, our aim is to qualitatively compare the various BTF slopes thus far obtained.

Several approaches have been pursued to recast the luminous (stars only) TF relation to one which also includes the gaseous disk mass component. The most common is to use baryonic mass instead of stellar luminosity (*e.g.*, McGaugh et al. 2000; Bell & de Jong 2001). In this approach, the mass of the stars is estimated by using a fixed stellar $\mathcal{M}/L$ (*e.g.*, McGaugh et al. 2000; Noordermeer & Verheijen 2007), or by modelling the luminous component with stellar population synthesis codes, *e.g.*, Bell & de Jong (2001), or by using mass models to fit rotation curves, (*e.g.*, McGaugh 2005). Another approach is to notionally convert the atomic gas to a luminosity (*e.g.*, Freeman (1999); Verheijen (2001)). Each method has its strength and weakness. For example, the assumption of a constant stellar $\mathcal{M}/L$ is simple, but it is known that the history of star formation is not uniform from one galaxy to the next and that stellar mass and luminosity of galaxies are sensitive to stellar population history effects (Bell & de Jong 2001). Converting gas to stars again requires adoption of an appropriate $\mathcal{M}/L$ ratio. Mass modelling, on the other hand is only possible for those galaxies with well measured (and behaved), H I rotation curves that extend out to large radii.

8.1. The slippery BTFR slope

In this section, we briefly discuss the measured BTFR slopes determined by various recent authors. Although some studies report slopes closer to 4, the reported slopes are mostly in the range 3.1 to 3.7 and most authors find that the BTFR is significantly flatter than the the TFR (stars only). At least some of the differences in slope come from different methodologies, including use of different kinematic indicators as well as assumptions about the stellar population histories used to calculate the $\mathcal{M}/L$ ratios. So here, we report on some of the results thus far:

Bell & de Jong (2001) use stellar population synthesis models to derive a slope (unweighted) for brighter disk galaxies of 3.51 ± 0.19, and argue that the BTFR slope would be even flatter if fainter disks were sub-maximal (as is widely believed).

In a study of disk galaxies in the Ursa Major cluster, Verheijen (2001) converts gas to luminosity and derives a range of BTFR slopes, between 3 and 4 for different gas conversion

values $\mathcal{M}_{gas}/L_{K'}$. He finds that a BTFR slope of 4 gives the least scatter when a constant $\mathcal{M}_{gas}/L_{K'} = 1.6$ is adopted. This result is based on calculating the reduced χ^2 values for different values of $\mathcal{M}_{gas}/L_{K'}$. We note however that the reduced χ^2 values in this analysis do not appear to pass through a minimum, so it is difficult to judge the significance of this result. Moreover, recent results by Noordermeer & Verheijen (2007), using the more common methodology of converting luminosity (K'-band) to baryon mass with a fixed stellar $\mathcal{M}/L$, for mostly the same galaxies yield a markedly flatter BTFR slope of 3.36 ± 0.1 and 3.04 ± 0.08 when the asymptotic rotational velocity and W_{20} are respectively used as the kinematic rotation value. This appears to be statistically significant and but in itself is a selection effect which we discuss towards the end of the paper.

Kassin et al. (2007) on the other hand use a different method that uses a kinematic estimator which accounts for disordered or non-circular gas motions. They obtain a 'TFR' slope of 3.3 ± 0.2 (lower panel of their fig 1) at low z and a fitted 'BTFR' slope slightly flatter than 3. It is noted however that some of their low mass galaxies are classified as disturbed or compact systems and that there may be a systematic effect since rotation curves from emission line data are likely to be still growing at the last measured point.

Geha et al. (2006) find an extremely flat BTFR slope of 1.89 ± 0.08 for their sample of SDSS dwarf galaxies. However when combined with brighter samples from the literature that include the Verheijen (2001) sample, the they find a BTFR slope of 3.70 ± 0.15, consistent with the BTFR LCDM slope predicted by Bullock et al. (2001) of 3.4 ± 0.1, similar to that found by Rijcke et al. (2007) who obtain a BTFR slope of ~ 3.2 using stellar population synthesis modelling to estimate the stellar mass component of their disks. When stellar population synthesis models are used to calculate the stellar mass component of galaxies, the derived BTFR slopes determined by authors are generally flatter and typically closer to the value of ~ 3 expected from ΛCDM cosmological simulations. However, some authors, do find slopes closer to 4. Stark et al. (2009) for example use rotation curve data to create a BTFR and argue that line widths are not accurate enough. Their sample consists of gas rich galaxies of intermediate baryon mass for which the flat part of the rotation curve is reached. They calculate BTFR slopes that are not much effected by the chosen stellar population model (IMF). Trachternach et al. (2009) obtain a BTFR slope consistent with 4 for a small sample of low mass galaxies but given the small baseline in rotational velocity, and that many of their rotation curves appear to still be rising at the last measured point, their data may also be consistent with a significantly different BTFR slope.

Meyer et al. (2008) use H I velocity width data and stellar $\mathcal{M}/L$ from stellar population synthesis modelling that include $\mathcal{M}/L$ values from Bell & de Jong (2001) as well as a recipe for gas mass that includes a molecular contribution. They find a slope near 4 but only for

galaxies with maximum rotational velocities > 100 km/s: see their fig. 14. These relatively massive galaxies would mostly have H I extending out to the flat part of the rotation curve. On the other hand, McGaugh (2005) also find a flat BTFR with slope of 3.37 ± 0.13 with stellar population synthesis models, without an additional IMF scaling. However McGaugh (2005) also compute significantly flatter BTFR slopes for their maximum stellar IMF scaling as well as with their maximum disk and their MOND modelled baryon masses and also report BTFR slopes ~ 4 (see their tab. 2).

As mentioned in Sec. 5 we examine the effect that scaling our modelled $\mathcal{M}/L$ values would have on the BTFR for the Sakai et al. (2000) galaxies. We find that if we scale our $\mathcal{M}/L$ by 1.5 and 2.0, weighted bivariate fits are produced with reduced $\chi^2 = 0.9$ that are significantly steeper, with slopes: 3.3 ± 0.3 and 3.5 ± 0.3, respectively. Even larger scalings, indicative of a significantly different IMF, are unlikely to be real given the agreement as shown in Figure 2 between our modelled $\mathcal{M}/L$ and those of Bell & de Jong (2001) who argue for a universal scaled Salpeter IMF by taking maximum disk dynamical constraints into account. However, some authors (*e.g.*, Meurer et al. 2009), argue for a non universal IMF and that the upper end of the IMF varies systematically with galaxy mass. If true, low luminosity galaxies may have less massive stars than high luminosity galaxies and this may imply that even more stellar mass is locked up in the dwarf galaxies than we have accounted for with our universal Chabrier IMF. This would seem to be partial evidence against the large $\mathcal{M}/L$ scalings that produce a steeper BTFR slope.

Although, some authors prefer to use the flat part of the rotation curve as their velocity estimator, rather than W_{20}, choosing galaxies for which the flat part of the rotation curve is observable provides a consistent estimate of rotation but it is itself a strong selection effect which most low-mass galaxies do not satisfy. Samples of low-mass galaxies for which the flat part of the rotation curve is observable are biased towards those for which the H I distribution is more extended relative to the halo scale length r_s: i.e. their H I is intrinsically more extended or they have more centrally concentrated halos with relatively smaller scale lengths r_s and relatively larger concentration parameters $c = r_{vir}/r_s$. We can speculate why such a bias could tilt the slope of the BTFR towards higher values (~ 4) as observed: for example, it is possible that a significant fraction of the hydrogen in these more extended low-mass galaxies is ionized by the metagalactic UV field. In any case, the existence of this selection effect needs to be recognized.

For the purposes of relating dark matter and baryonic matter via the BTFR, we should also ask whether the flat level of the rotation curve V_{flat} is the right velocity to use ? V_{flat} is unlikely to be a good estimator of the circular velocity V_{vir} at the virial radius. We know this from basic theory (*e.g.*, of NFW models) and from the observational work of Battaglia et al.

(2005) for our own Galaxy, which indicates that $V_{\text{flat}} > V_{\text{vir}}$. Is V_{flat} any better for estimating V_{vir} than V_{max} of the maximum H I velocity which determines W_{20}?

Even if $\mathcal{M}_{\text{baryons}} \propto V_{\text{flat}}^4$, how does that relate to the cosmological slope of the $\mathcal{M}_{\text{baryons}}$ vs V_{vir} relation ? For example, to reconcile the usual BTFR slope of 4 with the cosmological slope of 3, we would need $V_{\text{flat}} \propto V_{\text{vir}}^{3/4}$: $i.e.$, a systematic change in halo structure with V_{vir}. Most lower-mass galaxies have $V_{\text{max}} < V_{\text{flat}}$ while most higher-mass galaxies have $V_{\text{max}} \approx V_{\text{flat}}$. This observed trend of $V_{\text{max}}/V_{\text{flat}}$ could in fact make V_{max} ($i.e.$, via W_{20}) a more consistent estimator of V_{vir} than is V_{flat}. Relating V_{max} or V_{flat} to the V_{vir} remains an unsolved problem, and it is not clear which of V_{max} or V_{flat} is better for our problem of relating the BTFR to cosmology.

REFERENCES

Aaronson, M., & Mould, J. 1983, ApJ, 265, 1

Allen, P. D., & Shanks, T. 2004, MNRAS, 347, 1011

Barnes, D. G., et al. 2001, MNRAS, 322, 486

Battaglia, G., Helmi, A., Morrison, H., Harding, P., Olszewski, E. W., Mateo, M., Freeman, K. C., Norris, J., & Shectman, S. A. 2005, MNRAS, 364, 433

Begum, A., & Chengalur, J. N. 2003, A&A, 409, 879

Begum, A., Chengalur, J. N., Karachentsev, I. D., Kaisin, S. S., & Sharina, M. E. 2006, MNRAS, 365, 1220

Bell, E. F., & de Jong, R. S. 2000, MNRAS, 312, 497

Bell, E. F., & de Jong, R. S. 2001, ApJ, 550, 212

Broeils, A. H., & van Woerden, H. 1994, A&AS, 107, 129

Bruzual, G., & Charlot, S. 2003, MNRAS, 344, 1000

Burkert, A. 2003, Ap&SS, 284, 697

Bullock, J. S., Dekel, A., Kolatt, T. S., Kravtsov, A. V., Klypin, A. A., Porciani, C., &
   Primack, J. R. 2001, ApJ, 555, 240

Cayatte, V., van Gorkom, J. H., Balkowski, C., & Kotanyi, C.: 1990, AJ, 100, 604

Courteau, S., MacArthur, L. A., Dekel, A., van den Bosch, F., McIntosh, D. & Dale, D.
   2003, astroph/0310440

Courteau, S., & Rix, H. 1999, ApJ, 513, 561

Dalcanton, J. J., Yoachim, P., & Bernstein, R. A. 2004, ApJ, 608, 189

de Vaucouleurs, G., de Vaucouleurs, A., Corwin, Jr., H. G., Buta, R. J., Paturel, G., &
   Fouque, P. 1992, *VizieR Online Data Catalog*, 7137, 0

Eder, J. A., & Schombert, J. M. 2000, ApJS, 131, 47

Ferrarese, L., et al. 2000, ApJS, 128, 431

Freeman, K. C. 1970, ApJ, 160, 811

Freeman, K. C. 1999, in ASP Conf. Ser. 170: The Low Surface Brightness Universe, 3

Fukugita, M., & Peebles, P.J.E. 2006, ApJ, 639, 590

Geha, M., Blanton, M., Masjedi, M., & West, A. 2006, ApJ, 653, 240

Graham, J. A. PASP, 94, 244

Gurovich, S., McGaugh, S. S., Freeman, K. C., et al. 2004, in (Sydney: CSIRO), 412

Gurovich, S., McGaugh, S. S., Freeman, K. C., Jerjen, H., Staveley-Smith, L., & De Blok,
   W. J. G. 2004 PASA, 21, 412

Gurovich, S. 2007, Ph.D. thesis, Australian National University

Gurovich, S., Freeman, K. C. 2007, BAAA, 50, 251

Huchtmeier, W. K., & Richter, O. -G. 1989, A&A, 210, 1

Jedrzejewski, R. I. 1987, MNRAS, 226, 747

Kauffmann, G., et al. 2003, MNRAS, 341, 54

Kassin, S. A., et al. 2007, ApJ, 660, L35

Kennicutt, R. C., et al. 2003, PASP, 115, 928

Kilborn, V. A., et al. 2002, AJ, 124, 690

Koribalski, B. S., et al. 2004, AJ, 128, 16

Kravtsov, A., Gnedin, O., & Klypin, A. 2004, ApJ, 609, 482

Lang, R. H., et al. 2003, MNRAS, 342, 738

Maller, A. H., & Bullock, J. S. 2004, MNRAS, 355, 694

Macri, L. M., Huchra, J. P., Sakai, S., Mould, J. R., & Hughes, S. M. G. 2000, ApJS, 128, 461

Martin, M. C. 1998, A&AS, 131, 77

Mathewson, D. S., & Ford, V. L. 1996, ApJS, 107, 97

Meurer, G. R., et al. 2009, ApJ, 695, 765

Meyer, M. J., Zwaan, M. A., Webster, R. L., Schneider, S., & Staveley-Smith, L. 2008, MNRAS, 391, 1712

McGaugh, S. S., Schombert, J. M., Bothun, G. D., & de Blok, W. J. G. 2000, ApJ, 533, L99

McGaugh, S. S. 2005, ApJ, 632, 859

Mateo, M. 1998, ARA&A, 36, 435

Mo, H. J., & Mao, S. 2000, MNRAS, 318, 163

Navarro, J. F., & Steinmetz, M. 2000, ApJ, 538, 477

Noordermeer, E., & Verheijen, M. A. W. 2007, MNRAS, 381, 1463

Pierce, M. J., & Tully, R. B. 1992, ApJ, 387, 47

Pildis, R. A., Schombert, J. M., & Eder, J. A. 1997, ApJ, 481, 157

Pilyugin, L. S., Vílchez, J. M., & Contini, T. 2004, A&A, 425, 849

Press, W. H., Teukolsky, S. A., Vettering, W. T., & Flannery, B. P. 1992, Numerical Recipes in Fortran 77: The Art of Scientific Computing (2nd ed.; Cambridge: Cambridge Univ. Press), 660

Read, J. I., & Trentham, N. 2005, Royal Society of London Philosophical Transactions Series A, 363, 2693

Rijcke, S., Zeilinger, W., Hau, G., Prugniel, P., & Dejonghe, H. 2007, ApJ, 659, 1172

Sakai, S., et al. 2000, ApJ, 529, 698

Sandage, A. 1973, ApJ, 183, 711

Schlegel, D. J., Finkbeiner, D. P., & Davis, M. 1998, ApJ, 500, 525

Schröder, A., Drinkwater, M. J., & Richter, O.-G. 2001, A&A, 376, 98

Schombert, J. M. 2006, AJ, 131, 296

Stark, D. V., McGaugh, S. S., & Swaters, R. A. 2009, AJ, 138, 392

Swaters, R. A., Verheijen, M. A. W., Bershady, M. A., & Andersen, D. R. 2003, ApJ, 587, L19

Tassis, K., Kravtsov, A. V., & Gnedin, N. Y. 2008, ApJ, 672, 888

Tifft, W. G., & Huchtmeier, W. K. 1990, A&AS, 84, 47

Trachternach, C., de Blok, W. J., G., McGaugh, S. S., van der Hulst, J. M., and Dettmar, R .-J. 2009, A&A, 505, 507

Tremonti, C. A., et al. 2004, ApJ, 613, 898

Vallejo, O., Braine, J., & Baudry, A. 2002, A&A, 387, 429

van den Bosch, F. C. 2000, ApJ, 530, 177

Verheijen, M. A. W. 2001, ApJ, 563, 694

White, S. D. M. 1997, Galaxy Scaling Relations: Origins, Evolution and Applications, ed. L. N. da Costa & A. Renzini (New York: Springer), 3

Zwaan, M. A., van der Hulst, J. M., de Blok, W. J. G., & McGaugh, S. S. 1995, MNRAS, 273, L35

Table 1.   The H I quantities of the Sakai et al. (2000) galaxies

Galaxy	H I Flux $(\mathrm{Jy\,km\,s^{-1}})$	$\log W_{20}$(km/s)	References
M31	36732.2	2.74 ± 0.03	1, 2, 3
M33	13501.4	2.40 ± 0.07	1, 2, 3
NGC 925	328.5	2.42 ± 0.05	1, 2, 3, 4
NGC 1365	168.1	2.68 ± 0.04	2, 3, 5, 6, 7
NGC 1425	51.7	2.62 ± 0.04	4, 5, 6, 7
NGC 2090	125.3	2.50 ± 0.04	3, 5, 6
NGC 2403	1547.3	2.48 ± 0.06	1, 2, 3, 4
NGC 2541	145.1	2.37 ± 0.05	1, 2, 3
NGC 3031	795.4	2.72 ± 0.03	2, 3, 4, 8
NGC 3198	238.4	2.53 ± 0.03	1, 2, 3, 4
NGC 3319	83.1	2.41 ± 0.05	3, 9
NGC 3351	58.5	2.59 ± 0.05	1, 2, 3, 4
NGC 3368	81.5	2.67 ± 0.04	1, 3
NGC 3621	799.4	2.50 ± 0.04	2, 3, 4, 5
NGC 3627	41.7	2.63 ± 0.03	1, 3, 4
NGC 4414	67.7	2.74 ± 0.04	3, 10
NGC 4535	80.8	2.59 ± 0.04	3, 11, 12
NGC 4536	93.9	2.56 ± 0.03	3, 4
NGC 4548	12.2	2.62 ± 0.05	3, 11, 12
NGC 4725	110.2	2.67 ± 0.03	1, 2, 3, 4
NGC 7331	185.7	2.75 ± 0.02	1, 2, 3, 4, 13

References. — (1) Martin (1998); (2) Pilyugin et al. (2004); (3) de Vaucouleurs et al. (1992); (4) Kennicutt et al. (2003); (5) Koribalski et al. (2004); (6) Mathewson & Ford (1996); (7) Schröder et al. (2001); (8) Lang et al. (2003); (9) Broeils & van Woerden (1994); (10) Vallejo et al. (2002); (11) **?**; (12) Huchtmeier & Richter (1989); (13) Tifft & Huchtmeier (1990)

Table 2.   Photometrically derived quantities of the Sakai et al. (2000) galaxies

Galaxy	dist.	$\mathcal{M}$ gas	$\mathbf{M}_V$	$\mathbf{M}_I$	$\mathbf{M}_H$	[Fe/H]	h
M31[a,b,d]	0.77 ± 0.04	$6.43\,(1.71)\,\text{E}+09$	$\cdots$	-23.11 ± 0.18	-24.58 ± 0.11	-0.30 ± 0.50	$\cdots$
M33[a,b,d]	0.85 ± 0.04	$2.87\,(0.76)\,\text{E}+09$	$\cdots$	-19.84 ± 0.18	-21.06 ± 0.11	-0.46 ± 0.70	$\cdots$
NGC 925	9.29 ± 0.34	$9.37\,(2.44)\,\text{E}+09$	-20.10 ± 0.16	-20.67 ± 0.28	-21.91 ± 0.10	-0.73 ± 0.15	3.84
NGC 1365	18.97 ± 1.75	$2.00\,(0.62)\,\text{E}+10$	-22.34 ± 0.12	-23.40 ± 0.12	-25.05 ± 0.11	-0.32 ± 0.20	8.94
NGC 1425	23.01 ± 0.64	$9.05\,(2.32)\,\text{E}+09$	-21.44 ± 0.08	-22.39 ± 0.08	-23.82 ± 0.08	-0.28 ± 0.15	5.73
NGC 2090	12.30 ± 0.45	$6.26\,(1.63)\,\text{E}+09$	-20.27 ± 0.10	-21.30 ± 0.11	-22.70 ± 0.10	-0.48 ± 0.15	5.29
NGC 2403[a,b]	3.18 ± 0.35	$5.16\,(1.72)\,\text{E}+09$	$\cdots$	-20.38 ± 0.28	-21.89 ± 0.25	-0.48 ± 0.40	$\cdots$
NGC 2541	12.42 ± 0.46	$7.39\,(1.93)\,\text{E}+09$	-19.19 ± 0.13	-19.87 ± 0.13	-20.99 ± 0.10	-0.78 ± 0.15	3.76
NGC 3031[a,b]	3.63 ± 0.13	$3.46\,(0.90)\,\text{E}+09$	$\cdots$	-22.50 ± 0.17	-24.29 ± 0.10	-0.53 ± 0.15	$\cdots$
NGC 3198	14.45 ± 0.40	$1.65\,(0.42)\,\text{E}+10$	-20.78 ± 0.08	-21.56 ± 0.08	-22.97 ± 0.08	-0.68 ± 0.15	3.36
NGC 3319	14.32 ± 0.79	$5.63\,(1.54)\,\text{E}+09$	-19.72 ± 0.14	-20.33 ± 0.14	-21.19 ± 0.13	-0.90 ± 0.15	4.66
NGC 3351	10.05 ± 0.37	$1.95\,(0.51)\,\text{E}+09$	-20.61 ± 0.09	-21.64 ± 0.09	-23.31 ± 0.10	-0.04 ± 0.20	2.91
NGC 3368	10.96 ± 0.51	$3.24\,(0.86)\,\text{E}+09$	-21.31 ± 0.12	-22.31 ± 0.11	-24.16 ± 0.11	-0.08 ± 0.10	3.34
NGC 3621	6.70 ± 0.34	$1.19\,(0.32)\,\text{E}+10$	-20.16 ± 0.12	-21.06 ± 0.12	-22.59 ± 0.12	-0.53 ± 0.15	2.10
NGC 3627	10.28 ± 0.81	$1.46\,(0.43)\,\text{E}+09$	-21.79 ± 0.18	-22.66 ± 0.18	-24.25 ± 0.18	-0.03 ± 0.20	3.21
NGC 4414	19.14 ± 0.88	$8.20\,(2.19)\,\text{E}+09$	-21.60 ± 0.11	-22.61 ± 0.11	-24.40 ± 0.11	-0.08 ± 0.15	3.28
NGC 4535	16.60 ± 0.54	$7.35\,(1.90)\,\text{E}+09$	-21.42 ± 0.09	-22.28 ± 0.08	-23.47 ± 0.09	-0.08 ± 0.15	4.31
NGC 4536	15.49 ± 0.57	$7.44\,(1.94)\,\text{E}+09$	-21.05 ± 0.10	-21.95 ± 0.13	-23.54 ± 0.09	-0.43 ± 0.20	4.58
NGC 4548[c]	16.14 ± 1.71	$1.05\,(0.34)\,\text{E}+09$	-21.11 ± 0.23	-22.17 ± 0.23	$\cdots$	0.06 ± 0.15	3.09
NGC 4725	13.00 ± 0.48	$6.16\,(1.60)\,\text{E}+09$	-21.91 ± 0.09	-22.77 ± 0.09	-24.40 ± 0.10	-0.36 ± 0.15	5.39
NGC 7331	15.07 ± 0.69	$1.39\,(0.37)\,\text{E}+10$	-22.48 ± 0.11	-23.38 ± 0.11	-25.41 ± 0.11	-0.61 ± 0.15	5.74

For all tables when expressed in scientific notation, errors are in braces
NOTE: $6.43\,(1.71)\,\text{E}+09$ denotes $6.43 \times 10^9 \pm 1.71 \times 10^9$

Note. — Column (1) is the galaxy name; Column (2) is the adopted distance (in Mpc); Column (3) is the derived gas mass (in $\mathcal{M}_\odot$); Column (4) is the absolute V-band magnitude; Column (5) is the absolute I-band magnitude; Column (6) is the absolute H-band magnitude; Column (7) is adopted metallicity; Column (8) is the calculated scalelength (in kpc) determined from the V-band surface brightness profiles from Macri et al. (2000)
Unless indicated all [Fe/H] values calculated from Ferrarese et al. (2000)

[a] M_V unavailable in Sakai et al. (2000)

[b] Surface brightness data unavailable in Macri et al. (2000)

[c] Unreliable M_H in Sakai et al. (2000)

[d] [Fe/H] from Allen & Shanks (2004)

Table 3.   Evolutionary stellar population synthesis modelling for the Sakai galaxies from $(V - I)$ constrained simulations

Galaxy	$(\mathcal{M}/L_V)$	$(\mathcal{M}/L_I)$	$\mathcal{M}_{\text{stars}} : V$	$\mathcal{M}_{\text{stars}} : I$	$\mathcal{M}_{\text{total}} : V$	$\mathcal{M}_{\text{total}} : I$
NGC 925	0.82 ± 0.29	0.74 ± 0.20	$8.33\,(3.13)\,\text{E}+09$	$6.48\,(2.42)\,\text{E}+09$	$1.77\,(0.41)\,\text{E}+10$	$1.58\,(0.35)\,\text{E}+10$
NGC 1365	1.82 ± 0.26	1.34 ± 0.15	$1.45\,(0.35)\,\text{E}+11$	$1.44\,(0.32)\,\text{E}+11$	$1.65\,(0.38)\,\text{E}+11$	$1.64\,(0.36)\,\text{E}+11$
NGC 1425	1.45 ± 0.47	1.14 ± 0.26	$5.04\,(1.65)\,\text{E}+10$	$4.82\,(1.17)\,\text{E}+10$	$5.94\,(1.68)\,\text{E}+10$	$5.73\,(1.20)\,\text{E}+10$
NGC 2090	1.57 ± 0.37	1.20 ± 0.21	$1.85\,(0.52)\,\text{E}+10$	$1.87\,(0.38)\,\text{E}+10$	$2.47\,(0.56)\,\text{E}+10$	$2.49\,(0.43)\,\text{E}+10$
NGC 2403[a]	$\cdots$	$\cdots$	$\cdots$	$\cdots$	$\cdots$	$\cdots$
NGC 2541	0.63 ± 0.09	0.62 ± 0.07	$2.76\,(0.48)\,\text{E}+09$	$2.57\,(0.41)\,\text{E}+09$	$1.01\,(0.20)\,\text{E}+10$	$9.96\,(2.02)\,\text{E}+09$
NGC 3031[a]	$\cdots$	$\cdots$	$\cdots$	$\cdots$	$\cdots$	$\cdots$
NGC 3198	0.72 ± 0.12	0.68 ± 0.09	$1.36\,(0.25)\,\text{E}+10$	$1.34\,(0.21)\,\text{E}+10$	$3.01\,(0.50)\,\text{E}+10$	$2.98\,(0.48)\,\text{E}+10$
NGC 3319[b]	$\cdots$	$\cdots$	$\cdots$	$\cdots$	$\cdots$	$\cdots$
NGC 3351	1.72 ± 0.59	1.29 ± 0.33	$2.77\,(0.98)\,\text{E}+10$	$2.75\,(0.73)\,\text{E}+10$	$2.97\,(0.99)\,\text{E}+10$	$2.95\,(0.74)\,\text{E}+10$
NGC 3368	1.57 ± 0.27	1.22 ± 0.17	$4.83\,(0.97)\,\text{E}+10$	$4.81\,(0.82)\,\text{E}+10$	$5.15\,(0.99)\,\text{E}+10$	$5.14\,(0.84)\,\text{E}+10$
NGC 3621	1.16 ± 0.34	0.96 ± 0.21	$1.23\,(0.38)\,\text{E}+10$	$1.20\,(0.29)\,\text{E}+10$	$2.42\,(0.53)\,\text{E}+10$	$2.38\,(0.46)\,\text{E}+10$
NGC 3627	1.01 ± 0.19	0.88 ± 0.13	$4.84\,(1.20)\,\text{E}+10$	$4.78\,(1.06)\,\text{E}+10$	$4.99\,(1.22)\,\text{E}+10$	$4.93\,(1.07)\,\text{E}+10$
NGC 4414	1.62 ± 0.28	1.24 ± 0.15	$6.49\,(1.28)\,\text{E}+10$	$6.47\,(1.01)\,\text{E}+10$	$7.31\,(1.34)\,\text{E}+10$	$7.29\,(1.08)\,\text{E}+10$
NGC 4535	0.97 ± 0.17	0.85 ± 0.12	$3.32\,(0.62)\,\text{E}+10$	$3.28\,(0.50)\,\text{E}+10$	$4.05\,(0.66)\,\text{E}+10$	$4.01\,(0.55)\,\text{E}+10$
NGC 4536	1.11 ± 0.20	0.94 ± 0.12	$2.70\,(0.54)\,\text{E}+10$	$2.67\,(0.47)\,\text{E}+10$	$3.44\,(0.59)\,\text{E}+10$	$3.42\,(0.53)\,\text{E}+10$
NGC 4548	1.94 ± 0.28	1.43 ± 0.15	$4.97\,(1.29)\,\text{E}+10$	$4.95\,(1.19)\,\text{E}+10$	$5.08\,(1.31)\,\text{E}+10$	$5.06\,(1.21)\,\text{E}+10$
NGC 4725	0.95 ± 0.16	0.84 ± 0.11	$5.08\,(0.96)\,\text{E}+10$	$5.06\,(0.79)\,\text{E}+10$	$5.70\,(0.99)\,\text{E}+10$	$5.68\,(0.83)\,\text{E}+10$
NGC 7331	1.05 ± 0.24	0.90 ± 0.15	$9.50\,(2.35)\,\text{E}+10$	$9.51\,(1.85)\,\text{E}+10$	$1.09\,(0.24)\,\text{E}+11$	$1.09\,(0.19)\,\text{E}+11$

Note. — Column (1) is the galaxy name; Column (2) is the V-band $\mathcal{M}/L$ (in solar units); Column (3) is the I-band $\mathcal{M}/L$ (in solar units); Column (4) is the stellar mass (in solar units) derived from the V-band data; Column (5) is the stellar mass (in solar units) derived from the I-band data; Column (6) is the total mass (in solar units) derived using the V-band data; Column (7) is the total mass (in solar units) derived using the I-band data

[a]Not modeled: no V-band magnitude available from Sakai et al. (2000)

[b]Excluded: the model age is less than 8 Gyr

Table 4.   Evolutionary stellar population synthesis modelling for the Sakai galaxies from $(V - H)$ constrained simulations

Galaxy	$(\mathcal{M}/L_V)$	$(\mathcal{M}/L_H)$	$\mathcal{M}_{\mathrm{stars}}:V$	$\mathcal{M}_{\mathrm{stars}}:H$	$\mathcal{M}_{\mathrm{total}}:V$	$\mathcal{M}_{\mathrm{total}}:H$
NGC 925	0.69 ± 0.12	0.47 ± 0.07	6.95 (1.58) E +09	6.52 (1.17) E +09	1.63 (0.30) E +10	1.59 (0.28) E +10
NGC 1365	2.51 ± 0.49	0.88 ± 0.11	1.99 (0.55) E +11	2.19 (0.49) E +11	2.19 (0.58) E +11	2.39 (0.52) E +11
NGC 1425	1.47 ± 0.31	0.70 ± 0.12	5.08 (1.13) E +10	5.56 (1.07) E +10	5.99 (1.16) E +10	6.46 (1.11) E +10
NGC 2090	1.74 ± 0.36	0.74 ± 0.10	2.06 (0.53) E +10	2.09 (0.35) E +10	2.69 (0.57) E +10	2.72 (0.40) E +10
NGC 2403[a]	$\cdots$	$\cdots$	$\cdots$	$\cdots$	$\cdots$	$\cdots$
NGC 2541	0.69 ± 0.18	0.47 ± 0.09	3.03 (0.84) E +09	2.77 (0.57) E +09	1.04 (0.22) E +10	1.02 (0.21) E +10
NGC 3031[a]	$\cdots$	$\cdots$	$\cdots$	$\cdots$	$\cdots$	$\cdots$
NGC 3198	0.67 ± 0.12	0.46 ± 0.07	1.26 (0.25) E +10	1.69 (0.28) E +10	2.90 (0.50) E +10	3.33 (0.52) E +10
NGC 3319	0.72 ± 0.15	0.49 ± 0.08	5.10 (1.23) E +09	3.44 (0.70) E +09	1.07 (0.21) E +10	9.07 (1.82) E +09
NGC 3351	2.22 ± 0.45	0.79 ± 0.11	3.59 (0.79) E +10	3.95 (0.63) E +10	3.79 (0.79) E +10	4.15 (0.64) E +10
NGC 3368	2.80 ± 0.59	0.87 ± 0.13	8.61 (2.02) E +10	0.95 (0.17) E +11	8.94 (2.03) E +10	0.98 (0.17) E +11
NGC 3621	1.82 ± 0.36	0.76 ± 0.11	1.94 (0.43) E +10	1.96 (0.35) E +10	3.13 (0.58) E +10	3.15 (0.52) E +10
NGC 3627	1.53 ± 0.34	0.66 ± 0.14	7.34 (2.01) E +10	7.88 (2.06) E +10	7.49 (2.03) E +10	8.03 (2.07) E +10
NGC 4414	2.65 ± 0.41	0.86 ± 0.07	1.07 (0.20) E +11	1.16 (0.16) E +11	1.15 (0.20) E +11	1.25 (0.16) E +11
NGC 4535	0.83 ± 0.14	0.46 ± 0.06	2.83 (0.54) E +10	2.64 (0.38) E +10	3.56 (0.58) E +10	3.38 (0.45) E +10
NGC 4536	1.91 ± 0.37	0.76 ± 0.11	4.63 (0.98) E +10	4.69 (0.80) E +10	5.38 (1.02) E +10	5.43 (0.84) E +10
NGC 4548[b]	$\cdots$	$\cdots$	$\cdots$	$\cdots$	$\cdots$	$\cdots$
NGC 4725	1.87 ± 0.32	0.74 ± 0.10	9.99 (1.89) E +10	1.00 (0.16) E +11	1.06 (0.19) E +11	1.06 (0.16) E +11
NGC 7331[c]	$\cdots$	$\cdots$	$\cdots$	$\cdots$	$\cdots$	$\cdots$

Note. — Column (1) is the galaxy name; Column (2) is the V-band $\mathcal{M}/L$ (in solar units); Column (3) is the H-band $\mathcal{M}/L$ (in solar units); Column (4) is the stellar mass (in solar units) using the V-band data; Column (5) is the stellar mass (in solar units) using the H-band data; Column (6) is the total mass (in solar units) derived using the V-band data; Column (7) is the total mass (in solar units) derived using the H-band data

[a]Not modeled: no V-band magnitude available from Sakai et al. (2000)

[b]Not modeled: no H-band magnitude is available from Sakai et al. (2000)

[c]Unable to model: no model color exists as red as the observed given the metallicity

Table 5. Derived baryon masses of the Sakai galaxies

Galaxy	$\log \mathbf{W_{20}}$	$\mathcal{F}_{gas}$	$\mathcal{M}_{\mathbf{stars}}$	$\mathcal{M}_{\mathbf{total}}$	$\log \mathbf{\Sigma_{stars}}$	$\log \mathbf{\Sigma_{total}}$
NGC 925	2.42 ± 0.05	1.38 ± 0.40	$6.77\,(0.85)\,\mathrm{E}+09$	$1.63\,(0.16)\,\mathrm{E}+10$	1.86	2.25
NGC 1365	2.68 ± 0.04	0.12 ± 0.04	$1.64\,(0.20)\,\mathrm{E}+11$	$1.85\,(0.22)\,\mathrm{E}+11$	2.51	2.57
NGC 1425	2.62 ± 0.04	0.18 ± 0.05	$5.16\,(0.60)\,\mathrm{E}+10$	$6.06\,(0.62)\,\mathrm{E}+10$	2.40	2.47
NGC 2090	2.50 ± 0.04	0.32 ± 0.09	$1.98\,(0.21)\,\mathrm{E}+10$	$2.60\,(0.24)\,\mathrm{E}+10$	2.05	2.17
NGC 2403[a]	$\cdots$	$\cdots$	$\cdots$	$\cdots$	$\cdots$	$\cdots$
NGC 2541	2.37 ± 0.05	2.73 ± 0.75	$2.71\,(0.26)\,\mathrm{E}+09$	$1.02\,(0.10)\,\mathrm{E}+10$	1.48	2.06
NGC 3031[a]	$\cdots$	$\cdots$	$\cdots$	$\cdots$	$\cdots$	$\cdots$
NGC 3198	2.53 ± 0.03	1.18 ± 0.32	$1.39\,(0.12)\,\mathrm{E}+10$	$3.05\,(0.25)\,\mathrm{E}+10$	2.29	2.63
NGC 3319	2.41 ± 0.05	1.46 ± 0.89	$3.84\,(0.61)\,\mathrm{E}+09$	$9.77\,(1.39)\,\mathrm{E}+09$	1.45	1.85
NGC 3351	2.59 ± 0.05	0.06 ± 0.02	$3.38\,(0.38)\,\mathrm{E}+10$	$3.57\,(0.38)\,\mathrm{E}+10$	2.80	2.83
NGC 3368	2.67 ± 0.04	0.06 ± 0.02	$5.61\,(0.97)\,\mathrm{E}+10$	$5.95\,(0.98)\,\mathrm{E}+10$	2.91	2.93
NGC 3621	2.50 ± 0.04	0.78 ± 0.23	$1.52\,(0.21)\,\mathrm{E}+10$	$2.73\,(0.26)\,\mathrm{E}+10$	2.74	2.99
NGC 3627	2.63 ± 0.03	0.03 ± 0.01	$5.46\,(0.70)\,\mathrm{E}+10$	$5.61\,(0.71)\,\mathrm{E}+10$	2.93	2.94
NGC 4414	2.74 ± 0.04	0.10 ± 0.03	$7.90\,(1.27)\,\mathrm{E}+10$	$8.76\,(1.28)\,\mathrm{E}+10$	3.07	3.11
NGC 4535	2.59 ± 0.04	0.25 ± 0.07	$2.93\,(0.24)\,\mathrm{E}+10$	$3.69\,(0.27)\,\mathrm{E}+10$	2.40	2.50
NGC 4536	2.56 ± 0.03	0.23 ± 0.07	$3.17\,(0.49)\,\mathrm{E}+10$	$3.96\,(0.51)\,\mathrm{E}+10$	2.38	2.48
NGC 4548	2.62 ± 0.05	0.02 ± 0.01	$4.96\,(0.88)\,\mathrm{E}+10$	$5.07\,(0.89)\,\mathrm{E}+10$	2.92	2.93
NGC 4725	2.67 ± 0.03	0.10 ± 0.03	$6.05\,(1.14)\,\mathrm{E}+10$	$6.71\,(1.16)\,\mathrm{E}+10$	2.52	2.57
NGC 7331	2.75 ± 0.02	0.15 ± 0.05	$9.51\,(1.45)\,\mathrm{E}+10$	$1.09\,(0.15)\,\mathrm{E}+11$	2.66	2.72

[a]Not modeled: no V-band magnitude available from Sakai et al. (2000)

Note. — Column (1) is the galaxy name; Column (2) is the inclination corrected W_{20} (in $\mathrm{km\,s^{-1}}$); Column (3) is the gas–to–stars ratio ($\mathcal{M}_{\mathbf{gas}}/\mathcal{M}_{\mathbf{stars}}$); Column (4) is the stellar mass (in solar units); Column (5) is the gas plus stellar mass (in solar units); Column (6) is the mean stellar mass surface density (in $\mathcal{M}_\odot\,\mathrm{pc}^{-2}$); Column (7) is the mean baryon mass surface density (in $\mathcal{M}_\odot\,\mathrm{pc}^{-2}$)

Table 6.   Optical and near-IR surface photometry for the H<small>I</small> sample

Galaxy	μ_H	h_H	μ_V	h_V
HIPASS J1112-86	19.33	9.99	20.60	5.98
HIPASS J0554-71	19.00	5.43	21.76	5.65
HIPASS J1934-67	19.02	11.26	20.86	10.43
AM 0433-654	21.48	18.54	23.18	13.40
IC 5028	20.07	13.78	22.18	16.55
IC 5008	18.51	6.27	21.23	10.09
ESO 383- G 092	17.33	4.53	19.12	4.66
ESO 318- G 013	19.96	28.71	21.32	21.22
HIPASS J1801-72[a]	16.28	3.25	18.87	3.94
ESO 148- G 006	19.58	12.03	21.66	12.36
ESO 084- G 040	19.07	11.53	20.59	10.77
HIPASS J1424-16b	19.66	15.12	21.98	14.35
HIPASS J0736-74	18.60	6.58	20.04	5.85
ESO 085- G 088	20.72	49.03	22.57	38.57
SGC 0454.2-6138	20.30	11.59	22.34	13.51
ESO 052- G 010	19.60	8.14	21.21	7.77
ESO 321- G 014	20.49	25.72	20.97	11.81
HIPASS J0653-73	20.43	12.67	22.73	12.51
ESO 140- G 019	20.68	14.17	23.07	18.78
HIPASS J0039-76	18.07	5.40	20.23	6.18

Note. — Column (1) is the galaxy name; Column (2) is H-band disk central surface brightness (in mag arcsec^{-2}); Column (3) is the H-band scale length (in arcsec); Column (4) is the V-band disk central surface brightness (in mag arcsec^{-2}); Column (5) is the V-band scalelength (in arcsec)

[a]This galaxy appears to have a double exponential disk in the V-band

Table 7.   Photometric quantities of the H I selected sample

Galaxy	Incl.	V	H	V-H	V-H	V-H
HIPASS J1112-86	34.2	15.19 ± 0.07	12.77 ± 0.11	1.97	2.06	2.02 ± 0.08
HIPASS J0554-71	37.4	16.42 ± 0.09	13.98 ± 0.13	2.77	2.85	2.81 ± 0.11
HIPASS J1934-67	53.3	14.42 ± 0.06	12.40 ± 0.06	1.99	1.99	1.99 ± 0.07
AM 0433-654	42.9	15.97 ± 0.07	13.43 ± 0.10	2.18	2.24	2.21 ± 0.03
IC 5028	54.6	14.71 ± 0.08	13.01 ± 0.09	1.85	1.87	1.86 ± 0.10
IC 5008	72.7	15.05 ± 0.05	13.35 ± 0.07	2.15	2.13	2.14 ± 0.06
ESO 383- G 092	44.4	14.42 ± 0.03	12.79 ± 0.05	1.60	1.60	1.60 ± 0.06
ESO 318- G 013	71.3	14.16 ± 0.09	12.32 ± 0.12	1.51	1.55	1.53 ± 0.06
HIPASS J1801-72	49.5	14.37 ± 0.02	12.16 ± 0.05	2.41	2.45	2.43 ± 0.11
ESO 148- G 006	64.6	15.02 ± 0.08	12.99 ± 0.09	2.13	2.13	2.13 ± 0.20
ESO 084- G 040	48.1	14.38 ± 0.21	12.49 ± 0.06	1.65	1.72	1.69 ± 0.09
HIPASS J1424-16b	47.0	14.24 ± 0.19	12.28 ± 0.10	2.39	2.39	2.39 ± 0.09
HIPASS J0736-74	51.8	15.02 ± 0.06	13.26 ± 0.06	1.56	1.58	1.57 ± 0.19
ESO 085- G 088	54.0	13.89 ± 0.19	11.69 ± 0.26	1.95	2.08	2.02 ± 0.07
SGC 0454.2-6138	56.2	15.81 ± 0.12	13.99 ± 0.11	1.78	1.78	1.78 ± 0.07
ESO 052- G 010	49.5	15.37 ± 0.04	13.72 ± 0.06	1.70	1.70	1.70 ± 0.09
ESO 321- G 014	68.0	14.96 ± 0.06	12.65 ± 0.13	1.84	1.83	1.84 ± 0.08
HIPASS J0653-73	59.8	16.39 ± 0.10	13.87 ± 0.10	2.24	2.28	2.26 ± 0.06
ESO 140- G 019	56.9	15.77 ± 0.16	13.83 ± 0.13	2.10	2.14	2.12 ± 0.08
HIPASS J0039-76	53.9	14.67 ± 0.05	12.86 ± 0.07	1.83	1.83	1.83 ± 0.08

Note. — Column (1) is the galaxy name; Column (2) is the inclination (in degrees) derived with a q of 0.2; Column (3) is the V-band magnitude; Column (4) is the H-band magnitude; Column (5) is the color at the V-band half-light radius; Column (6) is the color at the H-band half-light radius; Column (7) is the adopted color from the mean of Columns (5) and (6)

Table 8. H I quantities from our narrow-band observations of the H I sample

Gal.	H I Flux (Jy km s^{-1})	$v_{hel.}$(km s^{-1})	logW_{20}(km s^{-1})	logW_{20}(km s^{-1})
HIPASS J1112-86	3.5	2187	1.86	2.11 ± 0.04
HIPASS J0554-71	3.6	1482	1.90	2.11 ± 0.04
HIPASS J1934-67	3.6	4123	2.27	2.37 ± 0.05
AM 0433-654	1.7	1229	1.65	1.82 ± 0.12
IC 5028	9.7	1619	2.10	2.19 ± 0.05
IC 5008	4.3	3714	2.26	2.28 ± 0.05
ESO 383- G 092	5.9	1410	1.86	2.02 ± 0.07
ESO 318- G 013	9.5	714	1.87	1.89 ± 0.04
HIPASS J1801-72	6.0	3284	2.35	2.47 ± 0.02
ESO 148- G 006	6.5	3167	2.24	2.28 ± 0.05
ESO 084- G 040	6.6	1235	1.95	2.08 ± 0.07
HIPASS J1424-16b	13.1	1487	1.93	2.08 ± 0.06
HIPASS J0736-74	2.2	1148	1.79	1.89 ± 0.09
ESO 085- G 088	4.4	1171	1.81	1.91 ± 0.05
SGC 0454.2-6138	2.1	972	1.79	1.87 ± 0.09
ESO 052- G 010	3.8	1387	2.00	2.11 ± 0.05
ESO 321- G 014	5.3	612	1.61	1.65 ± 0.14
HIPASS J0653-73	3.5	1205	1.99	2.05 ± 0.05
ESO 140- G 019	4.2	954	1.87	1.95 ± 0.07
HIPASS J0039-76	3.8	1754	1.97	2.06 ± 0.02

Note. — Column (1) is the galaxy name; Column (2) is the integrated H I flux; Column (3) is the measured heliocentric velocity; Column (4) is the observed W_{20} measurement (not corrected for inclination); Column (5) is the W_{20} measurement (corrected for inclination)

The error in the H I flux values are 15% determined by comparing our values with the independent H IPASS values. $v_{helio.}$ errors are $\simeq 5$ km s^{-1} and the errors of our W_{20} corrected values are between 5 and 20 km s^{-1}

Table 9.   Derived quantities of the H I selected sample

Galaxy	dist.	$\mathcal{M}_{\mathbf{gas}}$	$\mathbf{M}_V$	$\mathbf{M}_H$	[Fe/H]	h
HIPASS J1112-86	29.09 ± 4.36	9.79 (3.53) E+08	-17.13 ± 0.33	-19.55 ± 0.34	-0.86 ± 0.09	1.13
HIPASS J0554-71	19.75 ± 2.96	4.64 (1.67) E+08	-15.06 ± 0.34	-17.50 ± 0.35	-1.21 ± 0.07	0.53
HIPASS J1934-67	55.20 ± 8.28	3.62 (1.31) E+09	-19.29 ± 0.33	-21.31 ± 0.33	-0.48 ± 0.12	2.90
AM 0433-654	16.60 ± 2.49	1.55 (0.56) E+08	-15.13 ± 0.33	-17.67 ± 0.34	-1.20 ± 0.07	1.29
IC 5028	20.90 ± 3.14	1.40 (0.50) E+09	-16.90 ± 0.34	-18.59 ± 0.34	-0.90 ± 0.08	1.54
IC 5008	50.02 ± 7.50	3.55 (1.28) E+09	-18.45 ± 0.33	-20.25 ± 0.34	-0.63 ± 0.11	1.98
ESO 383- G 092	19.15 ± 2.87	7.15 (2.14) E+08	-16.99 ± 0.33	-18.62 ± 0.33	-0.88 ± 0.08	0.43
ESO 318- G 013	7.48 ± 1.12	1.75 (0.63) E+08	-15.21 ± 0.34	-17.05 ± 0.35	-1.18 ± 0.07	0.90
HIPASS J1801-72 [a]	44.25 ± 6.64	3.88 (1.40) E+09	-18.86 ± 0.33	-21.07 ± 0.33	-0.56 ± 0.12	0.77
ESO 148- G 006	42.95 ± 6.44	3.96 (1.43) E+09	-18.15 ± 0.34	-20.18 ± 0.34	-0.68 ± 0.10	2.54
ESO 084- G 040	16.74 ± 2.51	6.11 (2.20) E+08	-16.74 ± 0.39	-18.63 ± 0.33	-0.92 ± 0.09	0.90
HIPASS J1424-16b	22.90 ± 3.43	2.27 (0.82) E+09	-17.56 ± 0.38	-19.52 ± 0.34	-0.78 ± 0.10	1.64
HIPASS J0736-74	14.60 ± 2.19	1.55 (0.59) E+08	-15.80 ± 0.33	-17.56 ± 0.33	-1.08 ± 0.07	0.44
ESO 085- G 088	15.66 ± 2.35	3.56 (1.28) E+08	-17.08 ± 0.38	-19.28 ± 0.42	-0.86 ± 0.09	3.32
SGC 0454.2-6138	12.93 ± 1.94	1.16 (0.42) E+08	-14.75 ± 0.35	-16.56 ± 0.34	-1.26 ± 0.07	0.79
ESO 052- G 010	18.74 ± 2.81	4.41 (1.59) E+08	-15.99 ± 0.33	-17.65 ± 0.33	-1.05 ± 0.07	0.72
ESO 321- G 014	3.19 ± 0.48	1.78 (0.64) E+07	-12.55 ± 0.33	-14.87 ± 0.35	-1.64 ± 0.10	0.29
HIPASS J0653-73	15.53 ± 2.33	2.79 (1.01) E+08	-14.56 ± 0.34	-17.09 ± 0.34	-1.30 ± 0.07	0.95
ESO 140- G 019	11.64 ± 1.75	1.88 (0.68) E+08	-14.56 ± 0.36	-16.50 ± 0.35	-1.30 ± 0.08	0.93
HIPASS J0039-76	23.47 ± 3.52	6.91 (2.49) E+08	-17.19 ± 0.33	-18.99 ± 0.33	-0.85 ± 0.09	0.66

Note. — Column (1) is the galaxy name; Column (2) is the adopted distance (in Mpc); Column (3) is the gas mass (in solar units); Column (4) is the absolute V-band magnitude; Column (5) is the absolute H-band magnitude; Column (6) is the calculated metallicity; Column (7) is the calculated mean scalelength (in kpc) of the H and V-band exponential disks

[a]Appears to be a double exponential disk, using inner disk for scalelength calculation

– 30 –

Table 10.   Evolutionary stellar population synthesis for the H I galaxies from $(V - H)$ constrained simulations

Galaxy	$(\mathcal{M}/L_V)$	$(\mathcal{M}/L_H)$	$\mathcal{M}_{\mathbf{stars}}$:$V$	$\mathcal{M}_{\mathbf{stars}}$:$H$	$\mathcal{M}_{\mathbf{total}}$:$V$	$\mathcal{M}_{\mathbf{total}}$:$H$
HIPASS J1112-86	1.03 ± 0.22	0.62 ± 0.09	$6.75(2.53)\,\mathrm{E}+08$	$9.71(3.39)\,\mathrm{E}+08$	$1.65(0.55)\,\mathrm{E}+09$	$1.95(0.64)\,\mathrm{E}+09$
HIPASS J0554-71[a]	$\cdots$	$\cdots$	$\cdots$	$\cdots$	$\cdots$	$\cdots$
HIPASS J1934-67	0.76 ± 0.13	0.46 ± 0.06	$3.66(1.27)\,\mathrm{E}+09$	$3.60(1.19)\,\mathrm{E}+09$	$7.29(2.39)\,\mathrm{E}+09$	$7.23(2.34)\,\mathrm{E}+09$
AM 0433-654	1.75 ± 0.39	0.95 ± 0.18	$1.82(0.69)\,\mathrm{E}+08$	$2.61(0.95)\,\mathrm{E}+08$	$3.37(1.14)\,\mathrm{E}+08$	$4.16(1.40)\,\mathrm{E}+08$
IC 5028	0.82 ± 0.19	0.55 ± 0.09	$4.32(1.68)\,\mathrm{E}+08$	$3.52(1.23)\,\mathrm{E}+08$	$1.83(0.63)\,\mathrm{E}+09$	$1.75(0.60)\,\mathrm{E}+09$
IC 5008	1.08 ± 0.23	0.59 ± 0.09	$2.38(0.88)\,\mathrm{E}+09$	$1.75(0.60)\,\mathrm{E}+09$	$5.93(1.99)\,\mathrm{E}+09$	$5.30(1.77)\,\mathrm{E}+09$
ESO 383- G 092[b]	$\cdots$	$\cdots$	$\cdots$	$\cdots$	$\cdots$	$\cdots$
ESO 318- G 013	0.58 ± 0.04	0.49 ± 0.02	$6.52(2.08)\,\mathrm{E}+07$	$7.65(2.47)\,\mathrm{E}+07$	$2.41(0.81)\,\mathrm{E}+08$	$2.52(0.84)\,\mathrm{E}+08$
HIPASS J1801-72	1.86 ± 0.31	0.78 ± 0.10	$6.01(2.07)\,\mathrm{E}+09$	$4.94(1.64)\,\mathrm{E}+09$	$9.90(3.23)\,\mathrm{E}+09$	$8.83(2.85)\,\mathrm{E}+09$
ESO 148- G 006	1.13 ± 0.30	0.61 ± 0.11	$1.89(0.77)\,\mathrm{E}+09$	$1.70(0.62)\,\mathrm{E}+09$	$5.85(2.00)\,\mathrm{E}+09$	$5.66(1.91)\,\mathrm{E}+09$
ESO 084- G 040	0.83 ± 0.25	0.55 ± 0.11	$3.76(1.75)\,\mathrm{E}+08$	$3.66(1.33)\,\mathrm{E}+08$	$9.87(3.47)\,\mathrm{E}+08$	$9.77(3.26)\,\mathrm{E}+08$
HIPASS J1424-16b	1.82 ± 0.33	0.85 ± 0.13	$1.77(0.69)\,\mathrm{E}+09$	$1.30(0.45)\,\mathrm{E}+09$	$4.04(1.37)\,\mathrm{E}+09$	$3.57(1.18)\,\mathrm{E}+09$
HIPASS J0736-74	0.61 ± 0.11	0.49 ± 0.06	$1.18(0.42)\,\mathrm{E}+08$	$1.22(0.40)\,\mathrm{E}+08$	$2.73(0.90)\,\mathrm{E}+08$	$2.77(0.90)\,\mathrm{E}+08$
ESO 085- G 088	1.05 ± 0.34	0.62 ± 0.13	$6.58(3.11)\,\mathrm{E}+08$	$7.59(3.32)\,\mathrm{E}+08$	$1.01(0.39)\,\mathrm{E}+09$	$1.12(0.42)\,\mathrm{E}+09$
SGC 0454.2-6138	0.86 ± 0.18	0.64 ± 0.09	$6.24(2.39)\,\mathrm{E}+07$	$6.35(2.20)\,\mathrm{E}+07$	$1.78(0.60)\,\mathrm{E}+08$	$1.79(0.60)\,\mathrm{E}+08$
ESO 052- G 010	0.62 ± 0.08	0.48 ± 0.05	$1.42(0.47)\,\mathrm{E}+08$	$1.29(0.42)\,\mathrm{E}+08$	$5.83(1.97)\,\mathrm{E}+08$	$5.71(1.93)\,\mathrm{E}+08$
ESO 321- G 014	1.27 ± 0.27	0.94 ± 0.15	$1.23(0.46)\,\mathrm{E}+07$	$1.96(0.70)\,\mathrm{E}+07$	$3.02(1.01)\,\mathrm{E}+07$	$3.74(1.24)\,\mathrm{E}+07$
HIPASS J0653-73	1.51 ± 0.08	0.89 ± 0.04	$9.31(2.97)\,\mathrm{E}+07$	$1.43(0.45)\,\mathrm{E}+08$	$3.72(1.25)\,\mathrm{E}+08$	$4.22(1.39)\,\mathrm{E}+08$
ESO 140- G 019	1.73 ± 0.27	1.01 ± 0.14	$1.07(0.40)\,\mathrm{E}+08$	$9.51(3.35)\,\mathrm{E}+07$	$2.95(0.99)\,\mathrm{E}+08$	$2.83(0.95)\,\mathrm{E}+08$
HIPASS J0039-76	0.69 ± 0.13	0.48 ± 0.06	$4.79(1.70)\,\mathrm{E}+08$	$4.51(1.51)\,\mathrm{E}+08$	$1.17(0.39)\,\mathrm{E}+09$	$1.14(0.38)\,\mathrm{E}+09$

Note. — Column (1) is the galaxy name; Column (2) is the V-band $\mathcal{M}/L$ (in solar units); Column (3) is the H-band $\mathcal{M}/L$ (in solar units); Column (4) is the mass of stars (in solar units) using the stellar V-band data; Column (5) is the mass of the stars (in solar units) using the H-band data; Column (6) is the V-band stellar plus gas mass (in solar units); Column (7) is the H-band stellar plus gas mass (in solar units)

[a]Unable to model because no model $(V - H)$ exists as red as the observed given the input metallicity and color

[b]Ages younger than 8 Gyr

Table 11.   Derived baryon masses for the H I selected sample

Galaxy	$\log \mathbf{W_{20}}$	$\mathcal{F}_{gas}$	$\mathcal{M}_{stars}$	$\mathcal{M}_{total}$	$\log \mathbf{\Sigma_{stars}}$	$\log \mathbf{\Sigma_{total}}$
HIPASS J1112-86	2.11 (0.04)	1.25 (0.69)	7.81 (2.03) E+08	1.78 (0.42) E+09	1.99	2.35
HIPASS J0554-71[a]	$\cdots$	$\cdots$	$\cdots$	$\cdots$	$\cdots$	$\cdots$
HIPASS J1934-67	2.37 (0.05)	1.00 (0.60)	3.63 (0.87) E+09	7.26 (1.67) E+09	1.84	2.14
AM 0433-654	1.82 (0.12)	0.74 (0.56)	2.09 (0.56) E+08	3.68 (0.88) E+08	1.30	1.55
IC 5028	2.19 (0.05)	3.68 (1.32)	3.80 (0.99) E+08	1.79 (0.43) E+09	1.41	2.08
IC 5008	2.28 (0.05)	1.83 (0.82)	1.95 (0.50) E+09	5.58 (1.32) E+09	1.90	2.35
ESO 383- G 092[b]	$\cdots$	$\cdots$	$\cdots$	$\cdots$	$\cdots$	$\cdots$
ESO 318- G 013	1.89 (0.04)	2.51 (0.93)	6.99 (1.59) E+07	2.46 (0.58) E+08	1.13	1.68
HIPASS J1801-72[c]	2.47 (0.02)	0.72 (0.53)	5.36 (1.28) E+09	9.29 (2.14) E+09	3.16	3.40
ESO 148- G 006	2.28 (0.05)	2.23 (0.97)	1.77 (0.48) E+09	5.75 (1.38) E+09	1.64	2.15
ESO 084- G 040	2.08 (0.07)	1.66 (0.84)	3.69 (1.06) E+08	9.82 (2.38) E+08	1.86	2.28
HIPASS J1424-16b	2.08 (0.06)	1.58 (0.77)	1.44 (0.38) E+09	3.77 (0.90) E+09	1.93	2.35
HIPASS J0736-74	1.89 (0.09)	1.29 (0.67)	1.20 (0.29) E+08	2.75 (0.64) E+08	1.99	2.35
ESO 085- G 088	1.91 (0.05)	0.51 (0.52)	7.05 (2.27) E+08	1.06 (0.29) E+09	1.01	1.18
SGC 0454.2-6138	1.87 (0.09)	1.84 (0.83)	6.30 (1.62) E+07	1.79 (0.42) E+08	1.21	1.66
ESO 052- G 010	2.11 (0.05)	3.27 (1.12)	1.35 (0.31) E+08	5.77 (1.38) E+08	1.61	2.24
ESO 321- G 014	1.65 (0.14)	1.23 (0.69)	1.45 (0.39) E+07	3.31 (0.78) E+07	1.44	1.80
HIPASS J0653-73	2.05 (0.05)	2.58 (0.95)	1.08 (0.25) E+08	3.95 (0.93) E+08	1.28	1.84
ESO 140- G 019	1.95 (0.07)	1.88 (0.84)	1.00 (0.26) E+08	2.89 (0.68) E+08	1.26	1.73
HIPASS J0039-76	2.06 (0.02)	1.49 (0.72)	4.63 (1.13) E+08	1.16 (0.27) E+09	2.23	2.63

[a] and [b] same as in Tab. 10

Note. — Column (1) is the galaxy name; Column (2) is the inclination corrected W_{20} (in km s^{-1}); Column (3) is the gas–to–stars ratio ($\mathcal{M}_{\mathbf{gas}}/\mathcal{M}_{\mathbf{stars}}$); Column (4) is the stellar mass (in solar units); Column (5) is the gas plus stellar mass (in solar units); Column (6) is the mean stellar mass surface density (in $\mathcal{M}_{\odot}$ Mpc^{-2}); Column (7) is the mean baryon mass surface density (in $\mathcal{M}_{\odot}$ Mpc^{-2})

[c]Appears to be a double exponential disk, using inner disk in mean baryon mass surface density calculation

Table 12.   Parameters of the bivariate weighted fits (Press et al. 1992) for the TF/BTF relations with stellar $\mathcal{M}/L$ values calculated from population synthesis modelling and by using $\mathcal{M}/L$ values in braces, adopted from McGaugh et al. (2000).

Sample	TF slope	BTF slope	TF inter.	BTF inter.
H I & Sakai	$3.8\,(3.8) \pm 0.1\ (0.1)$	$3.2\,(3.3) \pm 0.1\ (0.1)$	$0.6\,(1.0) \pm 0.3\,(0.3)$	$2.5\,(2.4) \pm 0.3\,(0.3)$
H I	$3.4\,(3.2) \pm 0.3\ (0.3)$	$3.0\,(3.0) \pm 0.2\ (0.3)$	$1.5\,(2.2) \pm 0.5\,(0.6)$	$2.8\,(2.9) \pm 0.5\,(0.6)$
Sakai	$4.3\,(4.0) \pm 0.4\ (0.5)$	$3.1\,(3.2) \pm 0.3\ (0.3)$	$-0.6\,(0.3) \pm 1.0\,(1.2)$	$2.6\,(2.6) \pm 0.8\,(0.9)$

Note.   — Reduced Chi squared $(\chi^{2}_{\mathbf{red}})$ values for respective TF & BTF bivariate weighted fits: $1.8\,(1.4)\,\&\,1.3\,(1.2)\,,\,2.5\,(2.0)\,\&\,1.7\,(1.5)\,,\,0.9\,(0.7)\,\&\,0.9\,(1.0)$

Table 13.   mean baryon mass surface density (Σ_b) values for different disk scalings.

γ	1.0	1.5	2.0
$R_e/h_\star$	1.68	2.04	2.33
Σ_b	1.00	0.68	0.52
$\log\Sigma_b$	0.00	-0.17	-0.28

Note.   — γ values, defined as $h_{\mathrm{H\,I}}/h_\star$, R_e is the half light radius,: Increasing the $h_{\mathrm{H\,I}}$ scalelength for the dwarfs yields a $\log\Sigma_b$ *vs* $\log W_{20}$ slope of ~ 1.3 which goes in the right sense to flatten the BTFR
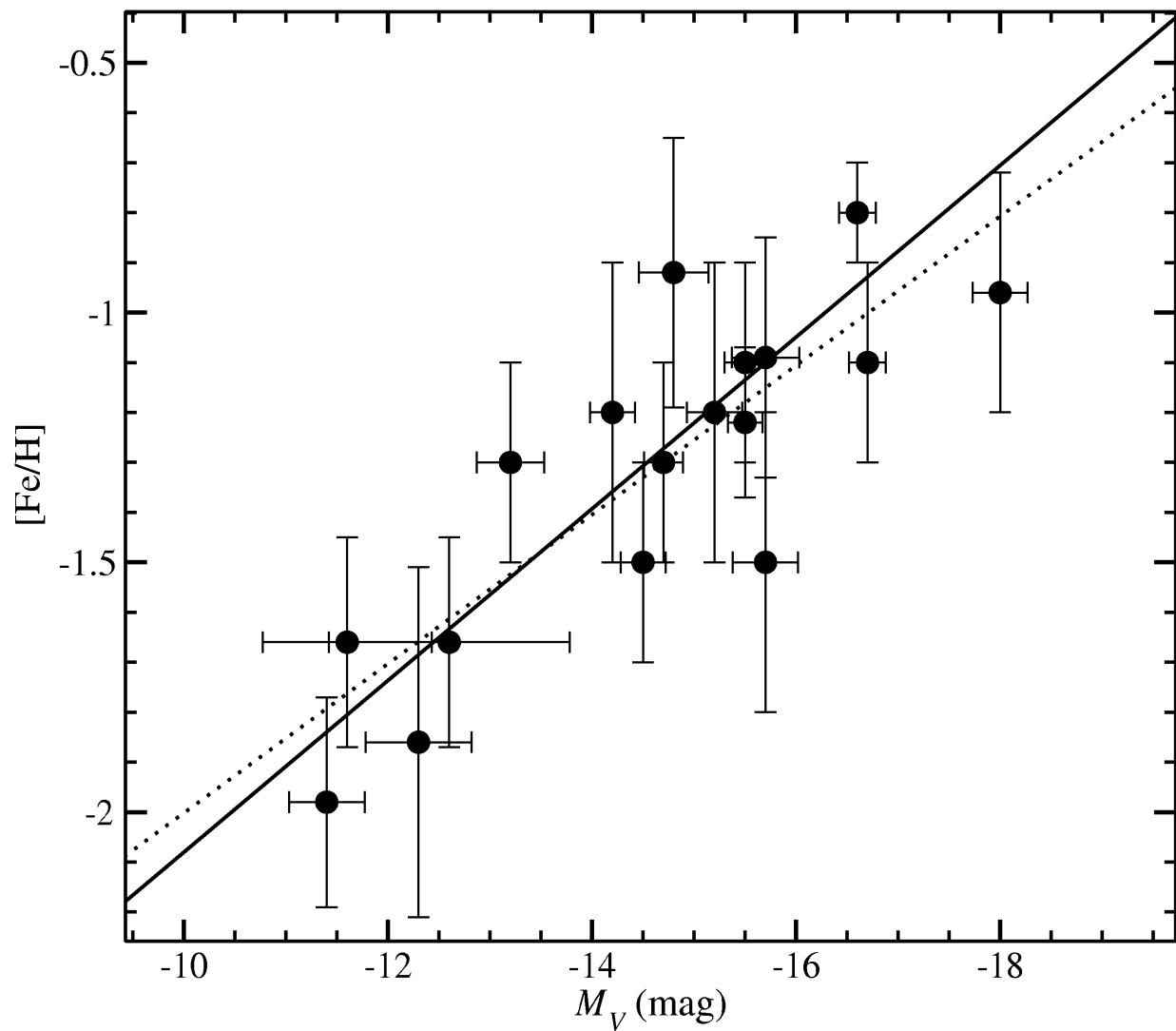
Fig. 1.— Adapted L-Z data for local group dwarf galaxies from Mateo 98. The weighted bivariate fit (solid line) shown is used to interpolate this relation for our galaxies.
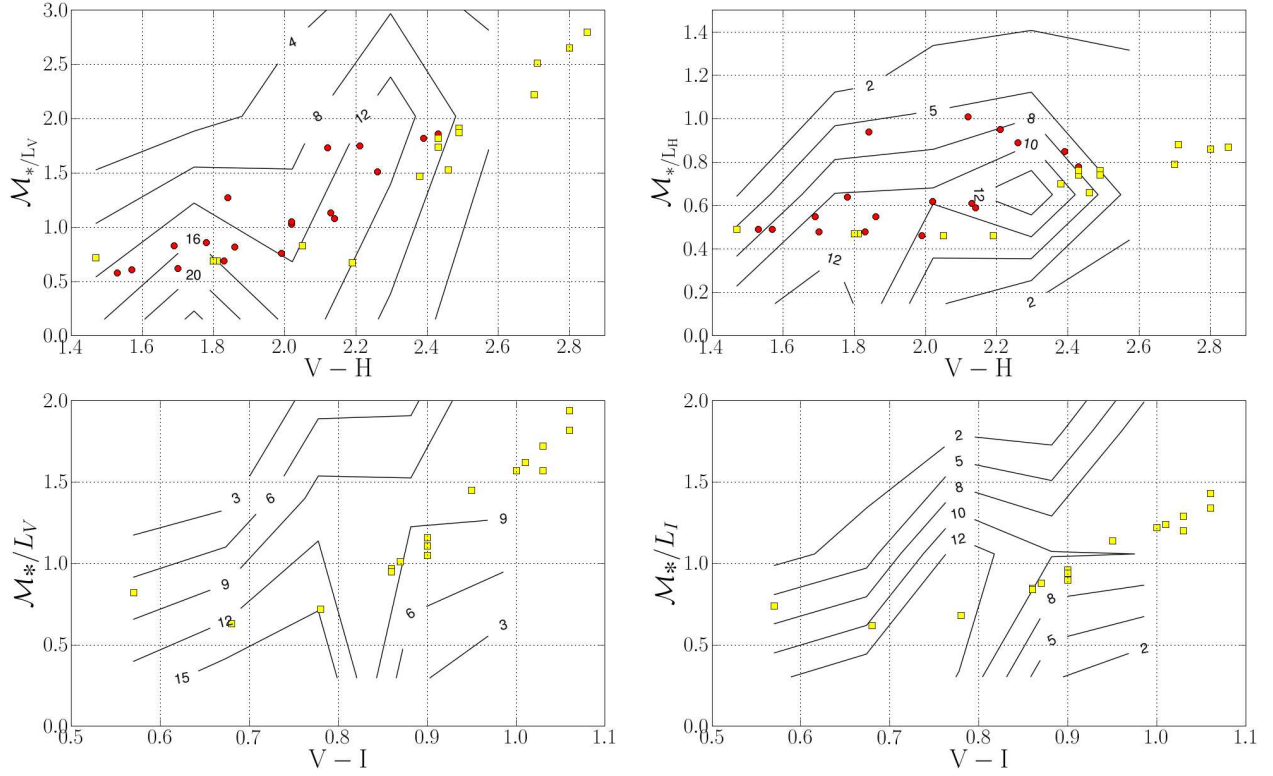
– 34 –

Fig. 2.— $\mathcal{M}/L$ *vs* color for the Sakai (yellow squares) and H I (red circles) samples with probability density of the Scaled Salpeter models (contours), from table 3 of Bell & de Jong (2001), constrained with our $(V-H)$ and $(V-I)$ colors
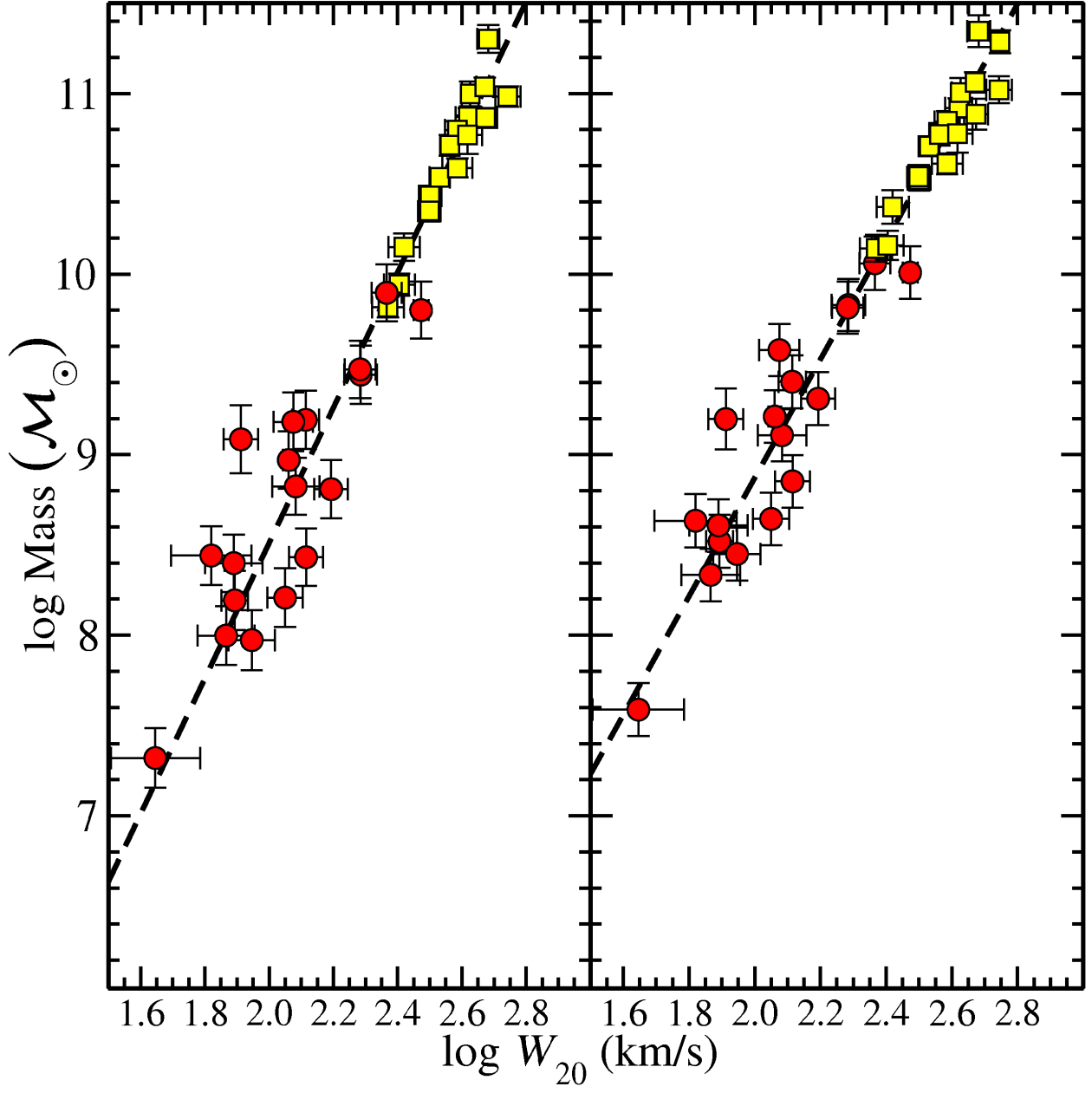
– 35 –

Fig. 3.— TF (left panel) and BTF (right panel) relations for the two samples of disk galaxies. Stellar masses (left panel) are shown with $\mathcal{M}/L$ values taken from McGaugh et al. (2000) for the H I selected (red circles), and Sakai et al. (2000) (yellow squares) with weighted bivariate fits (solid line). Weighted bivariate fits for the union of the H I and Sakai et al. (2000) galaxies are also shown (broken line).
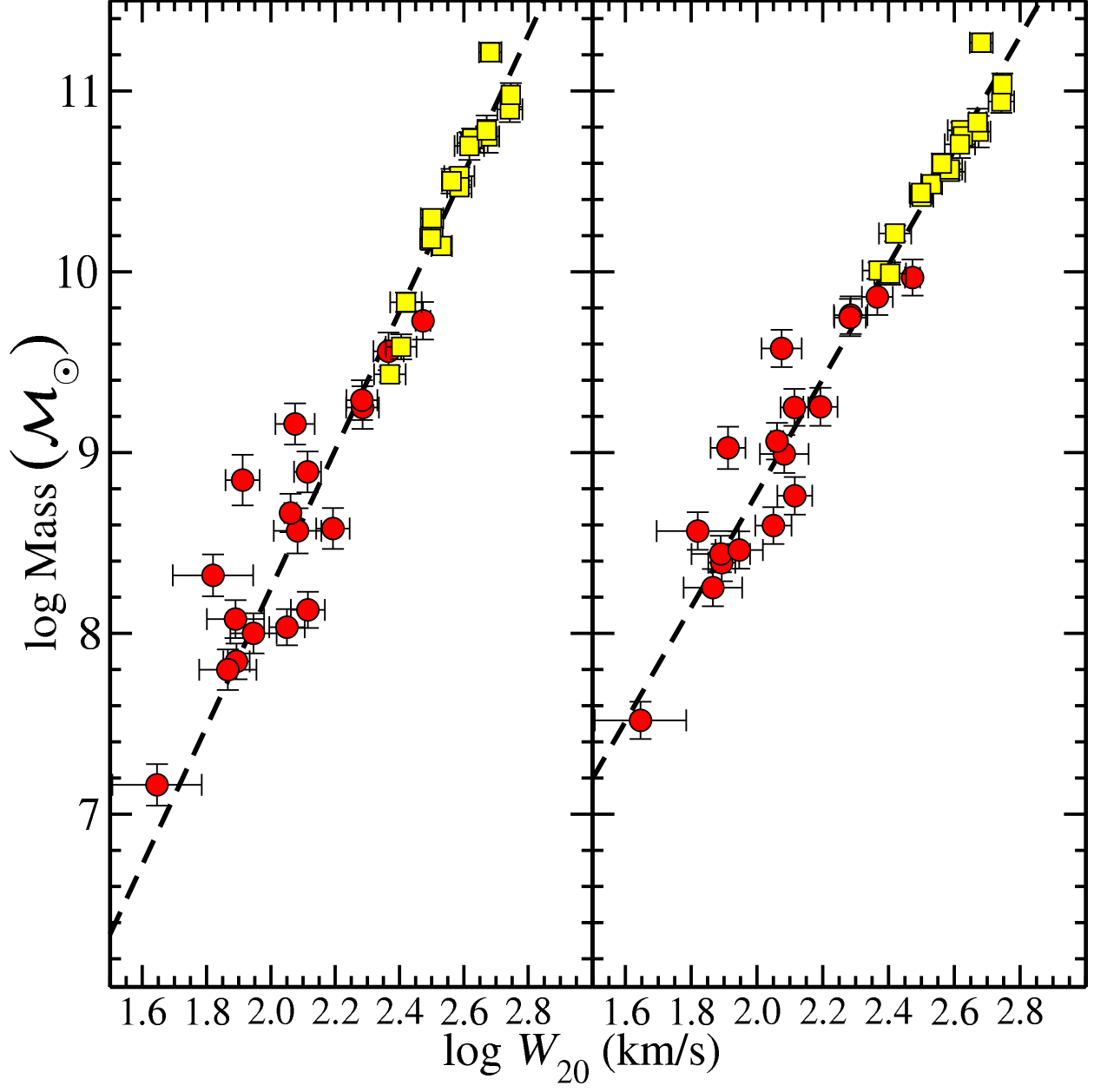
Fig. 4.— Same as Figure 4 but with stellar $\mathcal{M}/L$ values calculated from the simple stellar population synthesis models of Bruzual & Charlot (2003) with weighted bivariate fits (broken line).
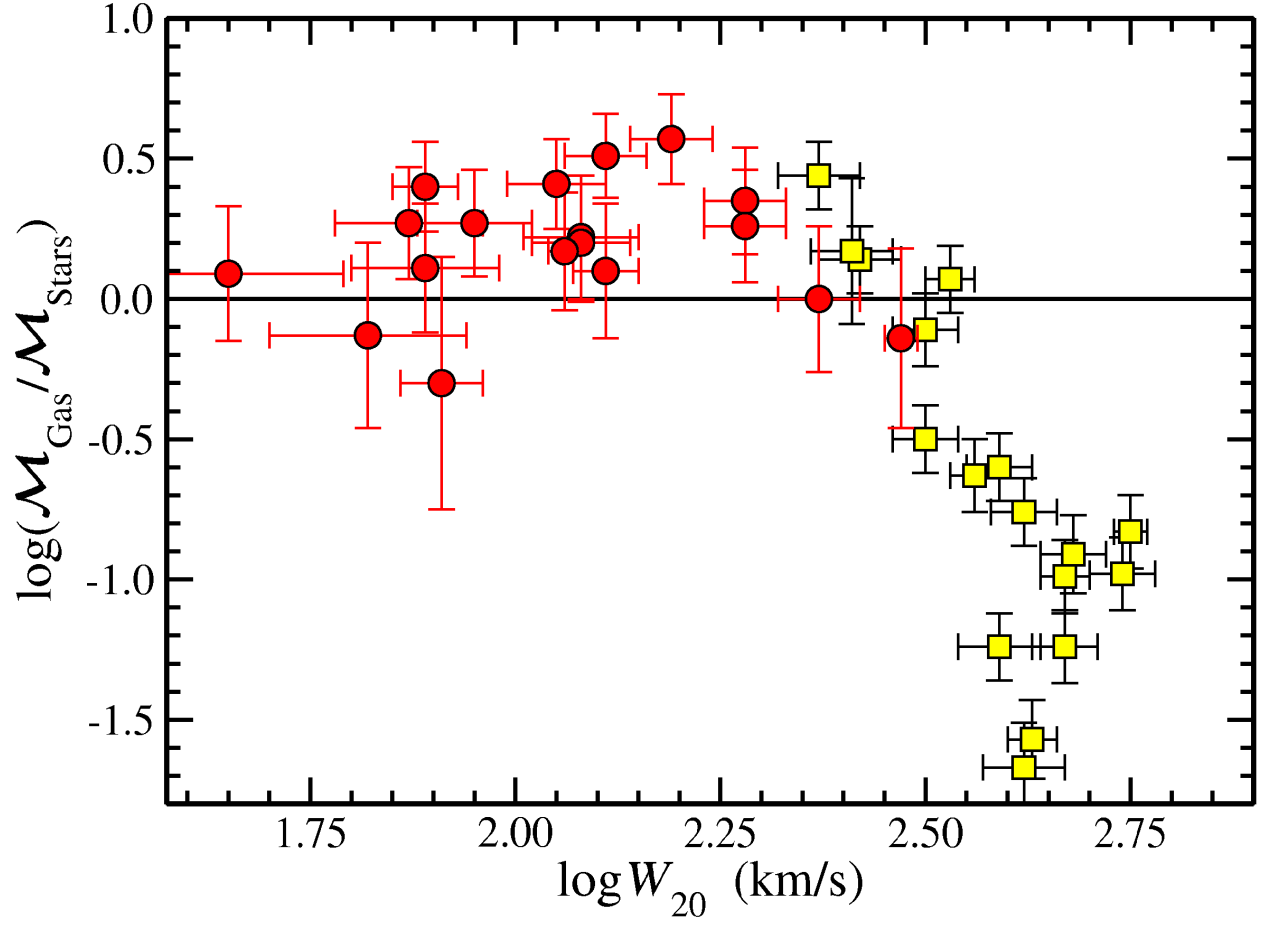
Fig. 5.— $\mathcal{M}_{gas}/\mathcal{M}_{stars}$ fraction *vs* W_{20} for the two samples of disk galaxies: H I selected (red circles), and Sakai et al. (2000) (yellow squares).
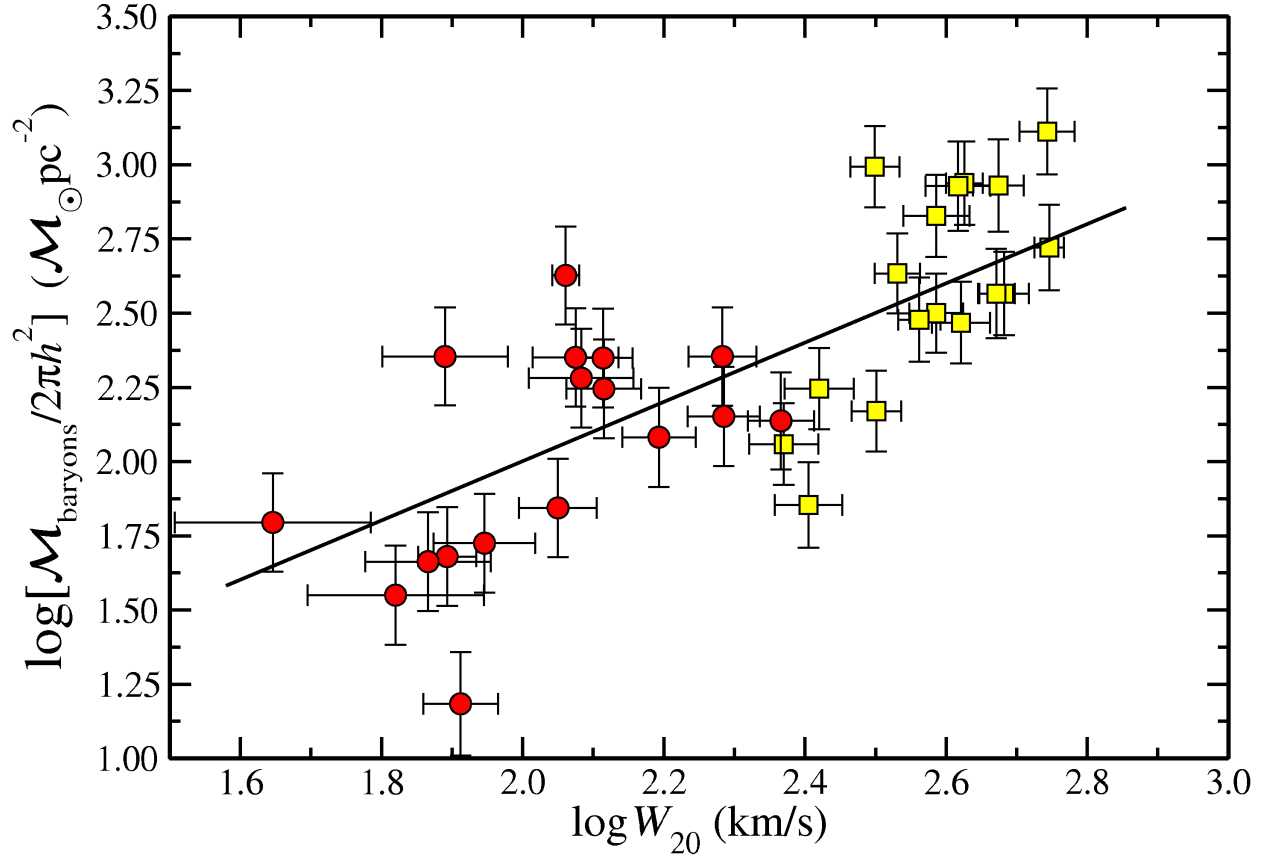
Fig. 6.— Mean baryon mass surface density *vs* W_{20} for the two samples of disk galaxies: H I selected (red circles) and Sakai et al. (2000) (yellow squares). A line with slope ~ 1 is shown, for comparison.